The Astrophysical Journal, 614:897–913, 2004 October 20

THE CRAB NEBULA AND PULSAR BETWEEN 500 GeV AND 80 TeV: OBSERVATIONS WITH THE HEGRA STEREOSCOPIC AIR CERENKOV TELESCOPES

F. Aharonian,[1] A. Akhperjanian,[2] M. Beilicke,[3] K. Bernlöhr,[1,4] H.-G. Börst,[5] H. Bojahr,[6] O. Bolz,[1] T. Coarasa,[7] J. L. Contreras,[8] J. Cortina,[7,9] S. Denninghoff,[7] M. V. Fonseca,[8] M. Girma,[1] N. Götting,[3] G. Heinzelmann,[3] G. Hermann,[1] A. Heusler,[1] W. Hofmann,[1] D. Horns,[1,10] I. Jung,[1] R. Kankanyan,[1] M. Kestel,[7] A. Kohnle,[1] A. Konopelko,[1,4] D. Kranich,[7] H. Lampeitl,[3] M. Lopez,[8] E. Lorenz,[7] F. Lucarelli,[8] O. Mang,[5] D. Mazin,[7] H. Meyer,[6] R. Mirzoyan,[7] A. Moralejo,[8] E. Oña-Wilhelmi,[8] M. Panter,[1] A. Plyasheshnikov,[1,11] G. Pühlhofer,[1,12] R. de los Reyes,[8] W. Rhode,[6] J. Ripken,[3] G. Rowell,[1] V. Sahakian,[2] M. Samorski,[5] M. Schilling,[5] M. Siems,[5] D. Sobzynska,[7,13] W. Stamm,[5] M. Tluczykont,[3,14] V. Vitale,[7] H. J. Völk,[1] C. A. Wiedner,[1] and W. Wittek[7]

Received 2004 June 2; accepted 2004 July 2

ABSTRACT

The Crab supernova remnant has been observed regularly with the stereoscopic system of five imaging air Cerenkov telescopes that was part of the High Energy Gamma Ray Astronomy (HEGRA) experiment. In total, close to 400 hr of useful data have been collected from 1997 to 2002. The differential energy spectrum of the combined data set can be approximated by a power law–type energy spectrum: $d\Phi/dE = \Phi_0(E/\mathrm{TeV})^{\Gamma}$, $\Phi_0 = \left(2.83 \pm 0.04_{\mathrm{stat}} \pm 0.6_{\mathrm{sys}}\right)10^{-11}$ photons cm^{-2} s^{-1} TeV^{-1}, and $\Gamma = -2.62 \pm 0.02_{\mathrm{stat}} \pm 0.05_{\mathrm{sys}}$. The spectrum extends up to energies of 80 TeV and is well matched by model calculations in the framework of inverse Compton scattering of various seed photons in the nebula, including for the first time a recently detected compact emission region at millimeter wavelengths. The observed indications for a gradual steepening of the energy spectrum in data is expected in the inverse Compton emission model. The average magnetic field in the emitting volume is determined to be $161.6 \pm 0.8_{\mathrm{stat}} \pm 18_{\mathrm{sys}}$ μG. The presence of protons in the nebula is not required to explain the observed flux, and upper limits on the injected power of protons are calculated to be as low as 20% of the total spin-down luminosity for bulk Lorentz factors of the wind in the range of 10^4–10^6. The position and size of the emission region have been studied over a wide range of energies. The position is shifted by 13″ to the west of the pulsar, with a systematic uncertainty of 25″. No significant shift in the position with energy is observed. The size of the emission region is constrained to be less than 2′ at energies between 1 and 10 TeV. Above 30 TeV the size is constrained to be less than 3′. No indication of pulsed emission has been found, and upper limits in differential bins of energy have been calculated reaching typically 1%–3% of the unpulsed component.

Subject headings: acceleration of particles — gamma rays: observations — gamma rays: theory — ISM: individual (Crab Nebula) — pulsars: individual (Crab pulsar)

Online material: color figure

1. INTRODUCTION

Observations of the Crab pulsar and Nebula have been carried out in every accessible wavelength band (ground- and space-based). The source has been established as a TeV emitter with the advent of ground-based Cerenkov imaging telescopes with sufficient sensitivity (Weekes et al. 1989). The broadband spectral energy distribution (SED) is exceptionally complete in coverage and unique among all astronomical objects observed and studied. The historical light curve of the supernova explosion of AD 1054 is not conclusive with respect to the type of progenitor star and leaves many questions concerning the stellar evolution of the progenitor star unanswered (Stephenson & Green 2002). At the present date, the observed remnant is of a plerionic type, with a bright continuum emission and filamentary structures emitting mainly in lines in the near-infrared and optical range.

The remaining compact central object is a pulsar with a period of 33 ms and a spin-down luminosity of $\propto\left(\dot{P}^3/P\right)5 \times 10^{38}$ ergs s^{-1}. The emitted power of the continuum peaks in the hard UV/soft X-ray band at $\approx 10^{37}$ ergs s^{-1} (assuming a distance of 2 kpc). Given that the kinetic energy of the spinning pulsar is the only available source of energy in the system, the spin-down luminosity is efficiently converted into radiation. There is no

[1] Max-Planck-Institut für Kernphysik, Postfach 103980, D-69029 Heidelberg, Germany.
[2] Yerevan Physics Institute, Alikhanian Brothers 2, 375036 Yerevan, Armenia.
[3] Universität Hamburg, Institut für Experimentalphysik, Luruper Chaussee 149, D-22761 Hamburg, Germany.
[4] Now at Humboldt-Universität, Institut für Physik, Newtonstrasse 15, Berlin, Germany.
[5] Universität Kiel, Institut für Experimentelle und Angewandte Physik, Leibnizstrasse 15-19, D-24118 Kiel, Germany.
[6] Universität Wuppertal, Fachbereich Physik, Gaussstrasse 20, D-42097 Wuppertal, Germany.
[7] Max-Planck-Institut für Physik, Föhringer Ring 6, D-80805 Munich, Germany.
[8] Universidad Complutense, Facultad de Ciencias Físicas, Ciudad Universitaria, E-28040 Madrid, Spain.
[9] Now at Institut de Física d'Altes Energies, Universidad Autonoma de Barcelona, Edifici Cn, E-08193 Bellaterra (Barcelona), Spain.
[10] Corresponding author; dieter.horns@mpi-hd.mpg.de.
[11] On leave from Altai State University, Dimitrov Street 66, 656099 Barnaul, Russia.
[12] Now at Landessternwarte Heidelberg, Königstuhl, Heidelberg, Germany.
[13] Home institute: University Lodz, Poland.
[14] Now at Laboratoire Leprince-Ringuet, École Polytechnique, Palaiseau, France (IN2P3/CNRS).

evidence for accretion onto the compact object as an alternative mechanism to feed energy into the system (Blackman & Perna 2004).

The emission of the Crab Nebula is predominantly produced by nonthermal processes (mainly synchrotron and inverse Compton), which form a continuum emission covering the range from radio to very high energy (VHE) gamma rays. The synchrotron origin of the optical and radio continuum emission was proposed by Shklovskii (1953) and experimentally identified by polarization measurements (Dombrovsky 1954).

The general features of the observed SED are characterized by three breaks, connecting four power law–type spectra. The breaks occur in the near-infrared, near-UV, and hard X-ray bands. The break frequencies are inferred indirectly because they occur in spectral bands that are difficult to observe. The high-energy part of the synchrotron spectrum cuts off at a few MeV. This energy is very close to the theoretical limit for synchrotron emission, derived from classical electrodynamics to be $h\nu_{\max} = \kappa m_e c^2/\alpha \approx \kappa 68$ MeV (independent of the magnetic field) with $\kappa \approx 1-3$, depending on the broadband spectrum of the emitting electrons (Aharonian 2000). In this sense, the Crab accelerates particles close to the possible limit. The synchrotron origin of multi-MeV photons requires the presence of electrons up to PeV energies. These PeV electrons inevitably radiate via inverse Compton scattering at photon energies up to and beyond 50 TeV, with detectable fluxes (Tanimori et al. 1998; Horns et al. 2003). Another independent indication for a common origin of MeV and 50–100 TeV photons is the possibly correlated variability of the nebula emission in these two energy bands, which has been discussed by Horns & Aharonian (2004).

In addition to the inverse Compton emission, other mechanisms might contribute to the VHE luminosity: (1) photons from π^0 decay from ions responsible for the acceleration of positrons at the termination shock (Arons 1995) and (2) bulk Comptonization of the relativistic wind (Bogovalov & Aharonian 2000).

The origin of the emitting particles is commonly assumed to be the pulsar, which efficiently accelerates a relativistic wind of particles (electrons/positrons and ions) in the proximity of the magnetosphere with a luminosity close to its spin-down luminosity. The relativistic wind terminates in a standing reverse shock, which is commonly associated with a ringlike feature identified at a distance of $\approx 4 \times 10^{17}$ cm, or $14''$, by recent X-ray observations (Weisskopf et al. 2000). At the position of the termination shock, the flow is dominated by kinetic energy. The orientation of the toroidal magnetic field is transverse to the flow direction and parallel to the shock surface (Rees & Gunn 1974). This shock geometry is not in favor of efficient acceleration of particles in shock drift or diffusive shock acceleration. Two possible alternative acceleration mechanisms have been discussed in detail in the literature.

A possible mechanism to accelerate particles in the relativistic wind is the dissipation of magnetic energy via reconnection of current sheets in the striped pulsar wind (Coroniti 1990), which was recently revisited by Kirk & Skjæraasen (2003). This mechanism was found to be close to the requirement to convert sufficiently rapidly the initially Poynting flux–dominated flow. However, it requires a rather high pair injection rate of 3×10^{40} s^{-1} and subsequently a small bulk Lorentz factor of the flow, less than 10^4.

An alternative process to efficiently accelerate particles at the shock, suggested by Arons (1995), invokes resonant scattering of positrons by cyclotron waves induced by the ions in the downstream region. Numerical particle-in-cell simulations (Hoshino et al. 1992) show that this mechanism produces a power law–type spectrum. The ions are expected to produce gamma rays after interacting with the matter in the nebula (Bednarek & Bartosik 2003; Amato et al. 2003) and produce signatures in the observed gamma-ray spectrum.

Independent of the actual acceleration mechanism, the injected nonthermal particle distribution in the nebula expands and cools adiabatically (Pacini & Salvati 1973) in a subsonic flow until it terminates at the envelope of the nebula. In the framework of the magnetohydrodynamic (MHD) flow model of Kennel & Coroniti (1984a), basic constraints on the bulk Lorentz factor of the wind and the pulsar's luminosity have been derived. It is noteworthy that in these models the radio emission is not explained, and an ad hoc assumption about an extra population of radio-emitting particles is required (Kennel & Coroniti 1984a; Atoyan & Aharonian 1996).

Furthermore, assuming that the MHD approximation holds, the downstream particle distribution, flow velocity, and magnetic field strength can be derived. Overall, the predicted synchrotron emission and its angular dimension in this model are in good agreement with observations (Kennel & Coroniti 1984b; Atoyan & Aharonian 1996).

The morphology of the nebula is resolved at most wavelengths. It is characterized by a complex structure and shows a general decrease of the size of the emission region with increasing energy. This is consistent with the decrease of the lifetime of electrons injected into the nebula with increasing energies. However, there are indications that at millimeter wavelengths, a compact, possibly nonthermal emission region is present that does not follow the general behavior (Bandiera et al. 2002). The central region close to the torus-like structure is also known to exhibit temporal variability at radio (Bietenholz et al. 2001), optical (Hester et al. 1995), and X-ray frequencies (Hester et al. 2002). The morphology of these moving structures, first seen in optical observations, has led to the commonly used term "wisps" (Scargle 1969), which are possibly (for a discussion see also Hester et al. 1995) explained by ions penetrating downstream of the standing shock and accelerating positrons and electrons via cyclotron resonance (Gallant & Arons 1994; Spitkovsky & Arons 2004). Whereas at radio wavelengths the measured spectrum is spatially constant over the entire nebula, at higher frequencies a general softening of the spectrum from the central region to the outer edge of the nebula is observed. This tendency is explainable by the short lifetime of the more energetic electrons. Recent high-resolution spectral imaging at X-ray energies have revealed a *hardening* of the spectrum in the torus region well beyond the bright ringlike structure that is usually identified with the standing relativistic shock (Mori et al. 2004). The spectral hardening at the torus could be indicative of ongoing acceleration far from the pulsar. In this case, the predictions for the size of the TeV emission region based on injection of electrons at the supposed standing reverse shock wave at the $14''$ projected distance are very likely underestimating the true size. The torus is located at $\approx 45''$ projected distance to the pulsar. Additional components, e.g., photons from π^0 decay, are expected to have roughly the same angular size as the radio nebula ($\approx 3'$), which is resolvable with stereoscopic ground-based Cerenkov telescopes.

Besides the nebula discussed above, the *pulsar* is a prominent source of pulsed radiation up to GeV energies (Bennett et al. 1977; Nolan et al. 1993). The characteristic bimodal pulse shape is retained over all wavelengths, with variations of the relative brightness of the two main components. The pulsar has

not been detected at energies beyond 10 GeV. Polar cap (Harding et al. 1978) and outer gap (Cheng et al. 1986) models have been successful at explaining the general features of the pulsed emission as curvature radiation of an energetic electron/positron plasma. The emission at TeV energies strongly depends on the location of the emission region. Generally, within polar cap models the optical depth for TeV photons is very large because of magnetic pair production processes. Effectively, the polar cap region is completely opaque to TeV emission. Within outer gap models, inverse Compton–scattered photons could be visible even at TeV energies. Again, the optical depth depends on the position of the outer gap in the magnetosphere. In any case, strong variation of the optical depth with energy results in rather narrow features in energy for a possible signal in a νf_ν diagram. This motivates a dedicated analysis searching for signals in narrow differential energy bins.

The paper is structured in the following way: After a description of the instrument (§ 2) and the data analyses (§ 3), results on the energy spectrum, morphology, and pulsed emission are given in § 4. Section 5 describes model calculations of the inverse Compton emission and compares the prediction with the measured energy spectrum. The average magnetic field in the emission region is derived, upper limits on the presence of ions in the wind are calculated, and additional components are discussed. Finally, a summary and conclusion are given (§ 6).

2. EXPERIMENTAL SETUP

Observations were carried out with the HEGRA (High Energy Gamma Ray Astronomy) stereoscopic system of five imaging air Cerenkov telescopes located on the Roque de los Muchachos on La Palma in the Canary Islands at an altitude of 2200 m above sea level. The system consisted of optical telescopes, each equipped with an 8.5 m^2 tessellated mirror surface, arranged in a Davies-Cotton design. The horizontal (altitude/azimuth) mounts of the telescopes were computer-controlled and could track objects in celestial coordinates with an accuracy of better than 25″ (Pühlhofer et al. 2003a). The telescopes were arranged on the corners of a square with a side length of 100 m, with a fifth telescope positioned in the center. The individual mirror dishes collected Cerenkov light generated by charged particles from air showers in the atmosphere, which produced an image of the short (a few nanoseconds' duration) light pulse in the focal plane. The primary focus was equipped with an ultrafast array of 271 photomultiplier tubes (PMTs) arranged in a hexagonal shape at $0\overset{\circ}{.}25$ spacing. The light collection area of the PMTs was enhanced by funnels installed in front of the photocathode. The camera covered a field of view with a full opening angle of $4\overset{\circ}{.}1$ in the sky, suitable for surveys (Konopelko et al. 2002; Rowell 2003; Pühlhofer et al. 2003b). The feasibility of survey-type observations is demonstrated by the first serendipitous discovery of an unidentified object with this instrument, named TeV J2035+4130 (Aharonian et al. 2002a).

The imaging air Cerenkov technique initially explored with single telescopes is improved by adding stereoscopic information to the event reconstruction. This was pioneered by the HEGRA group (see Aharonian 1993, Kohnle et al. 1996, and below). Stereoscopic observation improves the sensitivity, reducing background and achieving a low-energy threshold with a comparably small mirror surface, by efficiently rejecting local muon background events. An important benefit of the stereoscopy is also the redundancy of multiple images, allowing the efficient control of systematic uncertainties. In addition, the reconstruction of the energy and direction of the shower is substantially improved with respect to single-telescope imaging (Hofmann et al. 1999, 2000). Moreover, the probability of night-sky background triggers in two telescopes in coincidence is strongly reduced. The trigger condition for the telescope requires two adjacent pixels exceeding 6 photoelectrons (PEs) within an effective gate time of 14 ns.

Further details on the telescope hardware are given in Hermann (1995); a description of the trigger and readout electronics can be found in Bulian et al. (1998).

The telescope system, with four (from 1998 onward five) telescopes, was operational between spring 1997 and fall 2002.

3. DATA ANALYSES

3.1. *Data Taking*

Observations are taken in a "wobble" observation mode, in which the telescopes point at a position shifted by $0\overset{\circ}{.}5$ in declination to the position of the Crab pulsar. The sign of the shift is alternated every 20 minutes. All telescopes are aligned at the same celestial position and track the object during its transit in the sky. The wobble observation mode efficiently increases the available observation time while decreasing systematic differences seen between dedicated on- and off-source observations. The background for pointlike sources is estimated by using five off-source positions with an acceptance similar to that for the on-source observations (Aharonian et al. 2001a).

In the observation season 1998/1999, dedicated observations at larger zenith angles ($>45^\circ$) were performed in order to increase the collection area for high-energy events (typically above 10 TeV). All observations were carried out under favorable conditions with clear skies, low wind speeds (<10 m s^{-1}), and relative humidity below 100%.

The overall relative operation efficiency of the HEGRA system of Cerenkov telescopes reached 85% of the total available darkness time, so that 5500 hr of data on more than 100 objects and various scans (Aharonian et al. 2001b, 2002c) were collected in 67 months of operation. La Palma can be considered an excellent site for Cerenkov light observations, and moreover, the HEGRA system of Cerenkov telescopes was functioning very smoothly and reliably. The entire data set collected by the HEGRA system of telescopes has been used to search for serendipitous sources in the field of view (Pühlhofer et al. 2003b). Dedicated test observations of the Crab Nebula with a topological trigger, a reduced energy threshold, and a convergent pointing mode are reported elsewhere (Lucarelli et al. 2003).

3.2. *Data Selection*

Throughout the time of operation, the data acquisition (Daum et al. 1997b) and the electronics setup of the readout of the cameras and central triggering have remained unchanged. As a consequence of the upgrade from four to five telescopes in 1998 and occasional technical problems, the number of operational telescopes varies from three (5.5% of the total operational time) to four (38%) and five instruments (56%). Runs with fewer than three operational telescopes (0.5%) are not considered here. The selection of data aims at efficiently accepting good weather conditions with minimal changes in the atmosphere (mainly due to variations of the aerosol distribution).

The selection is based on the following approach: Under the assumptions that the cosmic-ray flux at the top of the atmosphere remains intrinsically constant and that the bulk of triggered events are cosmic-ray events, changes in the acceptance of the detector (mainly variations of the transparency of the atmosphere) should be easily seen in variations of the trigger rate. For individual data runs (20 minutes' duration), an expectation of the rate is calculated based on (1) the long-term average rate determined for every month (Pühlhofer et al. 2003a); (2) the change of rate with altitude; for $20^\circ < h < 60^\circ$: $R_{\rm cr}(h) = a_0 + a_1 h + a_2 h^2$, $a_0 = -6.363$, $a_1 = 0.556$, $a_2 = 0.004$; for $h > 60^\circ$: $R_{\rm cr} = \text{const.} = R_{\rm cr}(60^\circ)$; and (3) a scaling according to the number of operational telescopes ($R_5 : R_4 : R_3 = 1.16 : 1 : 0.8$). Runs with an average rate deviating by more than 25% from the expectation are rejected (15% of all runs available).

In Table 1, observational data are summarized for the individual (yearly) observational periods and for three intervals of zenith angle. The total amount of data accepted sums up to 384.86 hr, of which 20% were taken at large zenith angles.

TABLE 1
OBSERVATION TIMES

Season	[6.5°, 30°] (ks)	[30°, 45°] (ks)	[45°, 65°] (ks)	Total (ks)	Total (hr)
1997/1998	165.68	125.47	75.94	367.08	101.97
1998/1999	217.89	91.54	177.23	486.66	135.18
1999/2000	89.35	28.67	0.81	118.83	33.00
2000/2001	113.21	67.46	6.40	187.08	51.97
2001/2002	95.94	100.30	29.61	225.84	62.73
Total	682.07	413.43	289.99	1385.49	384.86

NOTE.—Data after selection for good weather.

3.3. *Data Calibration*

The long-term calibration of data and a deep understanding of the variations of detector performance over an extended period of time are essential for deriving a combined energy spectrum. The calibration methods used in this analysis are based on Pühlhofer et al. (2003a), with an additional relative intertelescope calibration (Hofmann 2003). The main steps for the calibration of image amplitude are briefly summarized below.

Calibration of image amplitude.—In order to study the *time dependence* of the telescopes' overall efficiency η (the ratio of the recorded amplitudes to the incident Cerenkov light intensity), it is convenient to factorize η into a constant efficiency η_0, according to the design of the telescopes at the beginning of operation, and time-dependent efficiencies $\eta_{\rm camera}(i)$ and $\eta_{\rm optics}(i)$, which are unity at the beginning of operation and are calculated for every month (period) i of operation:

$$\eta(i) = \eta_0 \eta_{\rm camera}(i) \eta_{\rm optics}(i). \quad (1)$$

The variation of the efficiency $\eta_{\rm optics}(i)$ is mainly caused by the aging of mirrors and, to some smaller extent, by aging of the light funnels installed in front of the PMTs, resulting in a loss of reflectivity at a steady rate of $-3.7\% \pm 0.3\%$ yr^{-1}. The variation of $\eta_{\rm camera}(i)$ is caused by aging of PMTs (rate of loss $-8.0\% \pm 0.3\%$ yr^{-1}) and occasional (typically twice per year) changes of high-voltage settings to compensate for the losses of efficiency. The two different efficiencies [$\eta_{\rm camera}(i)$, $\eta_{\rm optics}(i)$] are disentangled by calibrating the electronics' gain via special calibration events taken with a laser and studying the variation of the event rate for cosmic rays.

For the calibration of the electronics, a pulsed nitrogen laser mimics Cerenkov light flashes and allows the determination of flat-fielding coefficients to compensate for differences in the response and conversion factors of individual PMTs. The light is isotropized by a plastic scintillator material in the center of the dish and illuminates the camera directly. The conversion factors relating the recorded digitized pulse height to the number of PEs detected in the PMTs are derived from the relative fluctuations in the recorded amplitudes for these laser-generated calibration events.

Finally, the efficiency of the optical system (mirrors and funnels) is calculated indirectly: The laser calibration events are used to calculate an average electronics gain $\eta_{\rm camera}(i)$ for individual periods. By comparing the average cosmic-ray event rate with the expected value, an optical efficiency $\eta_{\rm optics}(i)$ is calculated.

This calibration method, based on the detected cosmic-ray rate, provides the possibility of regularly monitoring the detector efficiency in parallel with the normal operation of the telescopes. As a cross-check, muon runs have been performed, in which muon rings are recorded by the individual telescopes, with a modified single-telescope trigger. The muon rings provide an independent and well-understood approach to determining the efficiency of the telescope (Vacanti et al. 1994). The absolute value of the efficiency determined from the muon events is $\approx$11%, which is very close to the design specification of 12% used for the simulations. The muon events were taken at regular intervals and verify the decay of the reflectivity of the mirrors and the aging of the PMTs derived from the cosmic-ray rate. Further details on the calibration procedure for this data set are given in Pühlhofer et al. (2003a).

Intertelescope calibration.—The multitelescope view of individual events opens the possibility of intertelescope calibration. The method applied here follows Hofmann (2003), where for pairs of telescopes with a similar distance to the shower core, relative changes in the response are calculated. For the procedure, the data set was separated into five observation seasons coinciding with the yearly visibility period of the Crab Nebula. Events from an extended region in the camera (within $0.^\circ5$ radial distance to the center of the camera) passing the image shape selection criteria for gamma-ray events have been selected. In principle, the calibration can be performed using exclusively gamma-rays. The caveat with selecting only gamma-ray events is the comparably small number of events, which limits the statistical accuracy. With background events chosen from a large solid angle, the event statistics are sufficient to calculate the relative calibration factors within 1%–2% relative accuracy. Various systematic checks on simulated data and different gamma-ray sources have been performed to verify the systematic accuracy of the procedure to be within 2%.

3.4. *Data Reduction and Event Reconstruction*

Image cleaning.—The data are screened for defective channels (on average, 1% of the pixels are defective), which are subsequently excluded from the image analysis. Pixels exposed to bright starlight are excluded from the trigger during data taking and are subsequently not used for the image analysis. After pedestal subtraction and calibration of the amplitudes (see above), a static two-stage tail cut is applied, removing in the first step all pixels with amplitudes of less than 3 PEs and in the second step all pixels below 6 PEs unless a neighboring pixel has registered an amplitude exceeding 6 PEs.

TABLE 2
IMAGE AND EVENT SELECTION FOR DIFFERENT ANALYSES

Selection	Spectrum	Morphology	Pulsation
Angular distance to source, ϑ (deg)	<0.225	No cut	<0.118
Image shape, $\tilde{w}$	<1.1	<1.1	<1.1
Image amplitude (PEs)	>40	>40	>40
Image centroid position (deg)	<1.7	No cut	No cut
Estimated error on reconstructed event direction, σ_{xy} (deg)	No cut	<0.1 (0.06)[a]	No cut
Core position, r (m)	<200 (400)[b]	No cut	No cut
Stereo Angle, min (deg)	>20 (10)[c]	No cut	No cut
Number of images	≥ 3	≥ 2	≥ 2
Zenith angle (deg)	<65	<65	<65

[a] The cut on the estimated error for individual event direction, $\sigma_{xy} < 0.^{\circ}1$, is used when calculating the position of the emission region. The tighter cut ($\sigma_{xy} < 0.^{\circ}06$) is applied to data used to constrain the size of the emission region.
[b] For large zenith angles, the cut on the impact distance is relaxed ($r < 400$ m).
[c] For large zenith angles, the cut on the minimum stereo angle subtended between the major axes of the images in two telescopes is relaxed to 10°.

The tail-cut value is sufficiently high to ensure that the image is not contaminated by night-sky background–induced noise. The typical rms noise level varies between ≈ 0.8 and ≈ 1.5 PEs. Cleaned images exceeding a size of 40 PEs, and with a distance to the center of gravity of less than $1.^{\circ}7$ from the camera center, are combined in the stereoscopic analysis, which is used to reconstruct the shower parameters.

Image and event selection.—Selection of images and events are optimized separately for the three different studies carried out (spectrum, morphology, and pulsation). The selection applied for the energy spectrum is explained below. A summary of the different cuts applied for the different analyses is given in Table 2.

The cuts imposed on the reconstructed events to be used to determine the energy spectrum are chosen to minimize the systematic and statistical uncertainties while retaining enough sensitivity to reconstruct the energy spectrum at low (subthreshold) and high energies. In order to keep systematic uncertainties small, a loose angular cut is chosen (i.e., substantially larger than the angular resolution) on the half-angle of the event direction with respect to the source direction. Events with a half-angle $\vartheta < 0.^{\circ}225$ are retained.

The separation of gamma ray– and hadron-induced events is made by applying a cut on a parameter related to the width of the image: mean scaled width ($\tilde{w}$). This parameter is calculated for each event by scaling the width of individual images to the expectation value for a given impact distance of the telescope to the shower core, the size of the image, and the zenith angle of the event (Daum et al. 1997a). The individually scaled width values are averaged over all available images. For gamma-ray–like events this value follows a Gaussian distribution centered on an average of 1 with a width of 0.1. For this analysis, we choose a cut on $\tilde{w} < 1.1$, with an efficiency of 85% for gamma-ray events. The efficiency for gamma-ray events changes very little with energy and for different zenith angles.

Furthermore, the core position is required to be within 200 m of the central telescope. This cut is relaxed for events with a zenith angle of more than 45°, to 400 m, to benefit from the increased collection area for larger zenith angle events (Sommers & Elbert 1987; Konopelko et al. 2002). Finally, for the stereoscopic reconstruction, a minimum of three useful images and a minimum angle of 20° (10° for large zenith angles) subtended by the major axes of at least one of the pairs of images is required.

Event reconstruction.—The geometric reconstruction of multiple images of the same shower allows us to unambiguously reconstruct *event-by-event* the direction of the shower axis with a resolution of the angular distance of $0.^{\circ}06 = 3.'6$ for events with three or more images. The impact point of the shower is reconstructed in a similar way, and for a point source with known coordinates, the resolution for the shower impact point is better than 5 m (Hofmann et al. 1999; Aharonian et al. 2000a).

The stereoscopic observation method allows us to reconstruct the position of the maximum of the longitudinal shower development (Aharonian et al. 2000c), which is used to estimate the energy of the primary particle (Hofmann et al. 2000).

Whereas for single-telescope observations the reconstruction of the primary energy is influenced by the strong fluctuation of the longitudinal shower development and the subsequent variation of the measured light density in the observer's plane, the energy resolution for stereoscopic observations is improved by correcting for the fluctuation of the shower maximum. The relative energy resolution σ_E/E typically reaches values below 10% for energies above the threshold and moderately increases to 15% at threshold energies. Note that the bias of systematically overpredicting the energy at threshold is reduced considerably (conventional energy reconstruction produces a $\approx 40\%$ bias, whereas the improved method reduces this bias to $\approx 5\%$).

3.5. *Energy Spectrum*

The method of reconstructing the energy spectrum follows the approach described in Mohanty et al. (1998; also see Aharonian et al. 1999b). The method is considerably extended to deal with the temporal variations of the detector over the course of its lifetime (Aharonian et al. 2002b) and to improve on the extraction of weak signals (Aharonian et al. 2003a). The collection areas $A_{\rm eff}(E_{\rm rec}, \theta, i, n_{\rm tel})$ are derived from simulated air showers (Konopelko & Plyasheshnikov 2000), subject to a detailed detector simulation (Hemberger 1998). The same analysis chain as for the data is applied to simulated events.

The collection areas for five discrete zenith angles (0°, 20°, 30°, 45°, and 60°) are calculated as a function of reconstructed energy between 0.1 and 100 TeV. Moreover, the detector simulation is repeated for the 68 individual observation periods i (see § 3.3) using the temporal changes in efficiency as described above to model the variation of the response of the

detector. For each period and zenith angle, three individual simulations are performed with three, four, and five operational telescopes. In total, 1020 different collection areas are generated (five zenith angles, three telescope setups, 68 periods) and stored in a database.

For each individual event that is reconstructed and passes the event-selection criteria, a collection area is calculated. The procedure to interpolate the collection area for arbitrary zenith angles is described in detail in Aharonian et al. (1999b). The events are counted in discrete energy bins, and for each bin j covering the interval $(E,\ E + \Delta E)$ the differential flux is calculated:

$$\frac{d\Phi_j}{dE} = (T\Delta E)^{-1}\left[\sum \left(A_{\rm eff}^{\rm on}\right)^{-1} - \alpha \sum \left(A_{\rm eff}^{\rm off}\right)^{-1}\right]. \quad (2)$$

The factor α is given by the ratio of solid angles of the on and off observation regions: $\alpha = \Omega_{\rm on}/\Omega_{\rm off}$. For the observations considered here, five separate off regions with equal distance to the camera center are chosen ($\alpha = 0.2$).

For simplicity, the collection area above 30 TeV is assumed to be constant and equal to the geometrical size ($\pi 200^2$ m^2 for zenith angles smaller than 45°, $\pi 400^2$ m^2 for zenith angles beyond 45°). This has been checked with simulated air showers, as shown in Aharonian et al. (1999b).

The effective observation time T is calculated from the sum of the time differences of events. A correction for the dead time (2%) is applied, and occasional gaps in data taking (less than 0.5%) due to network problems are excluded from the effective observation time.

The resulting integrated fluxes calculated individually for the five different observing seasons show consistent values, with possible systematic differences smaller than 10% (see Fig. 1). The integrated fluxes above 1 and 5.6 TeV shown in Figure 1 are normalized to the respective integral fluxes calculated from the power-law fit to the entire spectrum. With the maximum deviation taken to be an estimate of systematic uncertainty, this translates into a possible variation of the absolute energy calibration of the system from year to year of less than 6%. As is already evident from Figure 1, the integrated flux above 5.6 TeV is on average slightly lower than the power-law fit expectation. This is an indication of a steepening of the energy spectrum toward higher energies, which is further discussed in § 5. At this point, the variations of the integral fluxes are consistent with systematic effects, and no temporal variation of the source can be claimed.

For the given constant energy resolution over a broad range of energies, systematic effects of bin-to-bin migration in the presence of a steeply falling spectrum are not important. With the use of an energy reconstruction method, which takes the height of the shower maximum into account (see § 3.4), systematic bias effects near the threshold are greatly reduced. In any case, the method applied automatically takes the effect of a small bias in the energy reconstruction into account.

The bin width in energy is chosen to reduce the interdependence of the bins ($\Delta E = 3\sigma_E$; σ_E is the typical energy resolution $\sigma_E/E \approx 10\%$), and therefore simple χ^2 minimization methods can be applied to fit arbitrary functions to the data. The errors on the parameters of the fit are calculated with the MINUIT package routines (James 1998) and have been tested with simple Monte Carlo–type simulations of random experiments. Bins with a signal exceeding 2 standard deviations according to equation (17) in Li & Ma (1983) have been included in the calculation of differential fluxes. Above 10 TeV, the bin width has been increased to compensate for the fast decrease of event statistics.

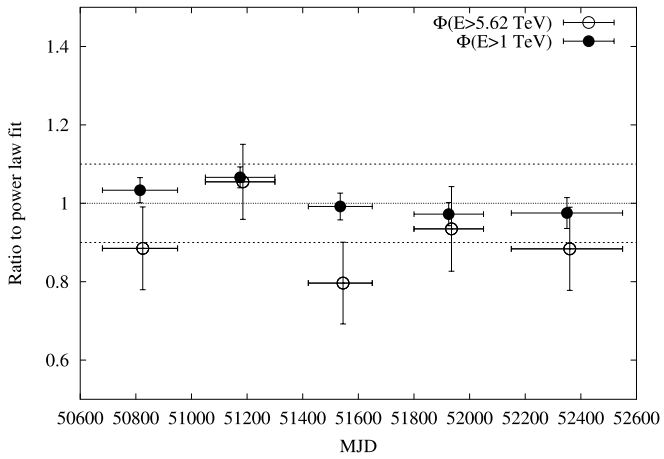

FIG. 1.—Integrated fluxes for the five observing years compared with each other, as a check for unnoticed temporal changes in the instrumental response. The respective values are normalized to the integral flux derived from the power-law fit to the entire data set. As is clearly seen from the relative deviations of $\Phi(E > 1$ TeV), systematic effects are smaller than 10%, indicated by the dashed lines, which translates into a relative uncertainty of the absolute energy calibration of better than 6% (assuming a power law–type spectrum with an index of −2.62). The integrated fluxes above 5.62 TeV show larger fluctuations that are still consistent with a constant flux.

3.6. *Position and Size of Emission Region*

In order to determine the position and size of the emission region, a two-dimensional Gaussian function (eq. [3]) is used to fit a histogram containing the arrival directions in discrete bins of 0.°05 side length in a projection of the sky. The bins are uncorrelated and chosen as a compromise between the systematic effect of discrete bins and sufficient statistics in the bins:

$$f(x,\ y) = f_0 \exp\left[-\frac{(x - \langle x\rangle)^2}{2\sigma_x^2} - \frac{(y - \langle y\rangle)^2}{2\sigma_y^2}\right] + f_{\rm ped}. \quad (3)$$

The coordinates (x, y) chosen are sky coordinates in declination (decl.) and right ascension (R.A.). The declination is measured in degrees, whereas right ascension is in units of hours. The constant pedestal $f_{\rm ped}$ is calculated from averaging the counts per bin in an annulus around the source region with inner radius 0.°2 and outer radius 0.°35.

The width of the distribution $\sigma_0 = \left(\sigma_x^2 + \sigma_y^2\right)^{1/2}$ is assumed to be symmetric ($\sigma_x = \sigma_y$) and a convolution of the instrumental point-spread function ($\sigma_{\rm PSF}$) and a source size ($\sigma_{\rm src}$): $\sigma_0 = \left(\sigma_{\rm PSF}^2 + \sigma_{\rm src}^2\right)^{1/2}$. This is a simplification assuming that the point-spread function and the source size are both following a Gaussian distribution (Aharonian et al. 2000a).

The analyses proceeds in two steps. In the first fit, a loose cut on the event selection is applied, rejecting events with an estimated angular resolution $\sigma_{xy} > 0.°10$, and the source extension is set to zero ($\sigma_0 = \sigma_{\rm PSF}$). In the second fit, the event selection is rejecting events with an estimated angular resolution $\sigma_{xy} > 0.°06$, and the source position is kept at the values found in the first fit, whereas $\sigma_{\rm src}$ is left as a free parameter.

The instrumental point-spread function $\sigma_{\rm PSF}$ is characterized using the predicted value of Monte Carlo simulations that have been checked against the performance for extragalactic objects, such as Mrk 421, Mrk 501, and 1ES 1959+650 (Aharonian

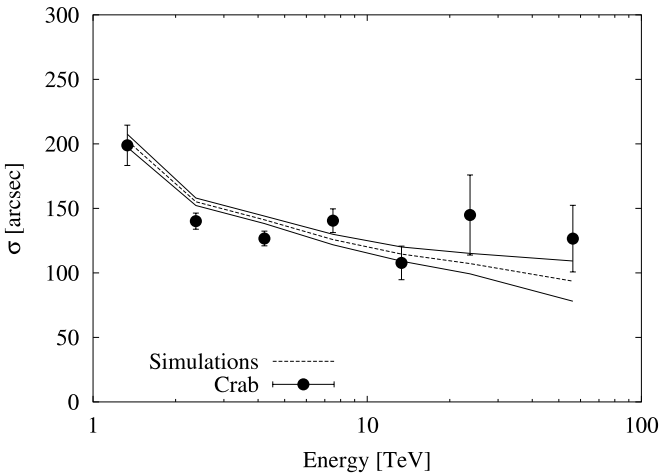

FIG. 2.—Point-spread function observed from the Crab Nebula. As a function of reconstructed energy, its size does not differ from the values predicted by simulations (dashed and solid lines indicate average and 1 σ uncertainty, respectively).

et al. 2003b). After a cut on the estimated error $\sigma_{xy} < 0.^{\circ}10$ is applied, selecting 75% of the gamma-ray events, the point-spread function is well described by a Gaussian function. The point-spread function weakly depends on the energy and the zenith angle after this selection cut is applied (see also Fig. 2).

Applying a dedicated analysis for high-energy events (e.g., raising the tail-cut values) improves the angular resolution at the high-energy end but requires reprocessing of all raw events. Given that systematic uncertainties of the pointing of the instrument (25″) and the low photon numbers at high energies strongly diminish the sensitivity for the source location and extension, a substantial improvement is not expected.

The size of the excess region is determined by fitting a Gaussian function (see eq. [3]) with a fixed position ($\langle x \rangle$, $\langle y \rangle$) to a histogram with the reconstructed arrival directions. As a compromise between diminishing statistics and small intrinsic point-spread function, a cut on $\sigma_{xy} < 0.^{\circ}06$ has been chosen that accepts 25% of the gamma-ray events and 3% of the background events. In Figure 2, the resulting size of the point-spread function is indicated, together with the prediction from simulations. In order to predict the size of the point-spread function, the simulated air showers have been weighted according to the distribution of zenith angles and energies found in data. The procedure has been checked against the point-spread function of Mrk 421 and Mrk 501 up to energies of 10 TeV. Based on the predictions and measurements, with their respective statistical uncertainties, upper limits on the source size are calculated with a one-sided confidence level (c.l.) of 99.865% (3 σ). Motivated by the absolute pointing accuracy, we have added a systematic uncertainty of 25″ to the upper limits. This can be considered a conservative estimate.

3.7. *Phase-resolved Analysis*

For events recorded after spring 1997, a global positioning system (GPS) time stamp is available for each individual event. With the high accuracy and stable timing of individual events, a coherent phase-resolved study of the arrival times over extended observation time is feasible.

In order to search for a pulsed signal from a pulsar that is not a part of a binary system, it is sufficient to use the arrival time at the barycenter of the solar system and to calculate a relative phase with respect to the arrival time of the main pulse as seen in radio observations. The conversion of the GPS time stamp to the solar barycenter uses the direction of the pulsar and the JPL DE200 solar system ephemeris (Standish 1982), which have a predicted accuracy of 200 m, confirmed by the updated DE405 ephemeris (Standish 1998; Pitjeva 2001). The algorithm applied includes a higher order correction for a relativistic effect that occurs whenever photons pass close to the Sun and are slightly deflected in the gravitational field (Shapiro 1964). The resulting delay, however, is, for the night-time observations of Cerenkov telescopes in any case, negligibly small.

The Crab pulsar ephemerides are taken from the public Jodrell Bank database (Lyne et al. 2003) and are used to calculate the relative phase of each event. A linear order Taylor expansion is used to calculate the arrival time of pulses for an arbitrary time between two radio measurements. For this purpose the derivative $\dot{P}$ of the period P is used in the expansion of the ephemerides. In the absence of glitches, this method gives accurate arrival times, with an accuracy of 250 μs. Whenever a glitch occurs with an abrupt change of P, a new interpolation period is started, taking the change in P and $\dot{P}$ into account.

The timing analysis has been checked with optical observations of the Crab pulsar using the prototype stand-alone Cerenkov telescope (Oña-Wilhelmi et al. 2003). In addition, data taken with the High Energy Spectroscopic System (HESS) instrument on the optical Crab pulses (Franzen et al. 2003) have been used to verify the procedure of the solar barycentric calculation.

Subsequent phase-folding of the HEGRA (on- and off-source) data results in a pulse profile. The pulse profile is split into bins, according to the pulse shape seen by the EGRET instrument (Fierro et al. 1998), using bins for the main pulse (P1), the leading and trailing wings of the main pulse (LW1, TW1), the bridge (B), the secondary pulse (P2) and its trailing and leading wings (LW2, TW2), and off-pulse (Off P).

A Pearson χ^2 test on a uniform distribution has some arbitrariness concerning the way that the phase distribution is discretized in bins. In addition to this bias, the sensitivity of the χ^2 test is inferior to that of tests invoking the relative phase information of successive events, such as the Rayleigh (Mardia 1972), Z_2^m (Buccheri et al. 1983), and H_2 tests (de Jager et al. 1989). Here, a Z_2^2 test has been applied that results in an improved sensitivity, with respect to the Rayleigh or χ^2 test statistics, for a sharp bimodal pulse form similar to the one seen by EGRET for the Crab pulsar.

The tests for periodicity are performed on seven energy intervals covering the energy from 0.32 to 100 TeV. This procedure is motivated by the predictions of sharp features in the spectrum of the pulsed emission (Hirotani & Shibata 2001).

4. RESULTS AND INTERPRETATION

4.1. *Energy Spectrum*

The reconstructed differential energy spectra for two different ranges in zenith angle are shown in Figure 3. Systematic uncertainties are estimated based on possible variations in the threshold region unaccounted for in the simulations and uncertainties in the nonlinear response of the PMTs and readout chain at high signal amplitudes. The range of systematic uncertainties is indicated by the gray shaded region in Figure 3. In addition to the energy-dependent uncertainties shown by the gray shaded region, the global energy scale is uncertain within 15%.

The dominating uncertainties are visible in the threshold region above 500 GeV. The estimate of the systematic

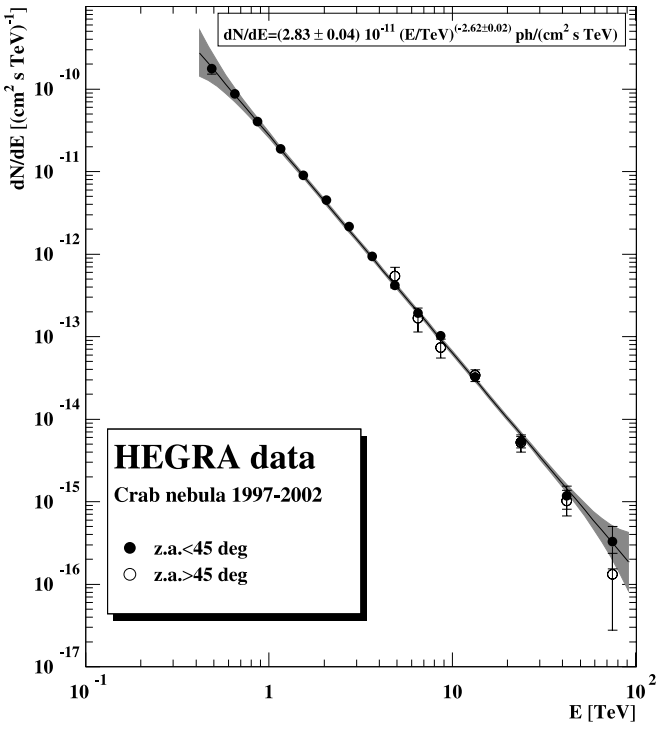

FIG. 3.—Differential energy spectrum, which covers the range from 0.5 to 100 TeV as a result of the spectral analysis in two different zenith angle intervals (6°.2–45°, 45°–65°). The significance of the data point centered on 86 TeV is 2.7 σ after the events from all zenith angles are combined. The shaded region indicates the range of systematic errors, which are most prominent in the threshold region, where the statistical errors are smaller than the systematic uncertainties.

uncertainties is shown to be quite conservative, judging from the smooth connection of the flux measured at small zenith angles with the flux measured at larger zenith angles at ≈6 TeV. The flux measured at the threshold for the data set with zenith angles larger than 45° is in very good agreement with the measurement from smaller zenith angles.

In additional, the good agreement of the two different energy spectra at very high energies shows that the systematic effect of the nonlinear response at high signal amplitudes is probably smaller than estimated. The nonlinear response affects mainly the small zenith angle observations, in which for a given energy of the shower the average image amplitude is much higher (by a factor of 4–6) than for larger zenith angles. The effect of the saturation/nonlinearity is expected to be negligible at larger zenith angles. The good agreement shows that the correction applied to the high signal amplitudes is accurate.

For the purpose of combining data taken at different zenith angles, the same approach as described in Aharonian et al. (2000b) is followed. The combined energy spectrum (Table 3) is well approximated by a pure power law of the form $d\Phi/dE = \Phi_0(E/\mathrm{TeV})^{\Gamma}$, with $\Phi_0 = (2.83 \pm 0.04_{\mathrm{stat}} \pm 0.6_{\mathrm{sys}}) \times 10^{-11}$ photons cm^{-2} s^{-1} TeV^{-1} and $\Gamma = -2.62 \pm 0.02_{\mathrm{stat}} \pm 0.05_{\mathrm{sys}}$. The $\chi^2_{\mathrm{red}}(\mathrm{dof}) = 1.3(13)$ indicates that deviations from a power law do not appear to be very significant. The systematic errors quoted on the parameters are the result of varying the data points within the systematic errors (the gray shaded band in Fig. 3), and for the normalization Φ_0 the uncertainty of the energy scale is included.

Even though a power-law fit to the data is a good approximation without statistically significant deviations, a systematic deviation from a power law in the form of a steepening can be seen upon closer inspection (see also Fig. 11) and is discussed in § 5.3.

4.2. *Source Position and Morphology*

In a previous HEGRA paper (Aharonian et al. 2000a), the emission size region of the Crab Nebula for energies up to 5 TeV has been constrained with a smaller data set (about one-third of the data used here) to be less than 1′.7. Here results from a similar analysis technique are presented. The most noticeable difference with respect to the previously published results is that the upper limits are calculated within seven independent energy bins covering the energy range from 1 to 80 TeV. In principle, an ionic component in the wind could be a rather narrow feature in the energy spectrum and therefore

TABLE 3
DIFFERENTIAL ENERGY SPECTRUM

$\langle E \rangle$ (TeV)	$E_{\mathrm{low}} - E_{\mathrm{high}}$ (TeV)	$d\Phi/dE \pm \sigma_{\mathrm{stat}}$ [(cm^2 s TeV)$^{-1}$]	N_{on}	N_{off}[a]	S[b] (σ)
0.365	0.316–0.422	$(1.97 \pm 1.17) \times 10^{-10}$	105	333	3.9
0.487	0.422–0.562	$(1.76 \pm 0.24) \times 10^{-10}$	369	705	14.1
0.649	0.562–0.750	$(8.78 \pm 0.53) \times 10^{-11}$	1012	1356	29.8
0.866	0.750–1.000	$(4.02 \pm 0.13) \times 10^{-11}$	2119	2108	50.0
1.155	1.000–1.334	$(1.87 \pm 0.09) \times 10^{-11}$	2829	2772	58.2
1.540	1.334–1.778	$(9.05 \pm 0.26) \times 10^{-12}$	2458	2220	56.1
2.054	1.778–2.371	$(4.51 \pm 0.12) \times 10^{-12}$	2017	1600	48.9
2.738	2.371–3.162	$(2.16 \pm 0.07) \times 10^{-12}$	1510	1114	47.3
3.652	3.162–4.217	$(9.33 \pm 0.36) \times 10^{-13}$	950	645	38.6
4.870	4.217–5.623	$(4.18 \pm 0.20) \times 10^{-13}$	579	330	31.7
6.494	5.623–7.499	$(1.93 \pm 0.12) \times 10^{-13}$	345	187	23.3
8.660	7.499–10.000	$(1.02 \pm 0.07) \times 10^{-13}$	238	111	21.4
13.335	10.000–17.783	$(3.28 \pm 0.31) \times 10^{-14}$	414	420	19.7
23.714	17.783–31.622	$(5.28 \pm 0.70) \times 10^{-15}$	150	242	10.2
42.170	31.622–56.234	$(1.10 \pm 0.25) \times 10^{-15}$	69	141	5.7
74.989	56.234–100.000	$(2.05 \pm 1.01) \times 10^{-16}$	36	104	2.7

[a] The value N_{off} is the sum of the background events in five discrete background regions: $\langle N_{\mathrm{off}} \rangle = N_{\mathrm{off}}/5$.
[b] The significance is calculated for the number of excess events $N_{\mathrm{on}} - \langle N_{\mathrm{off}} \rangle$ and invoking eq. (17) of Li & Ma (1983) with $\alpha = 0.2$.

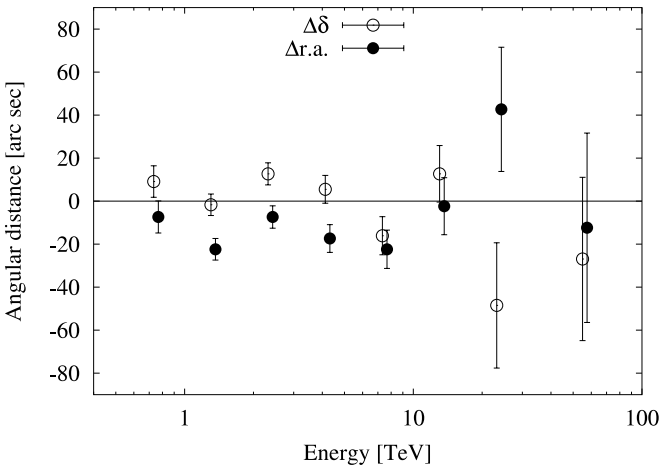

FIG. 4.—Position of the emission region as a function of reconstructed energy; it does not show significant variation. Open symbols indicate the deviation of the reconstructed declination to the declination of the pulsar, and filled symbols indicate the deviation of the right ascension.

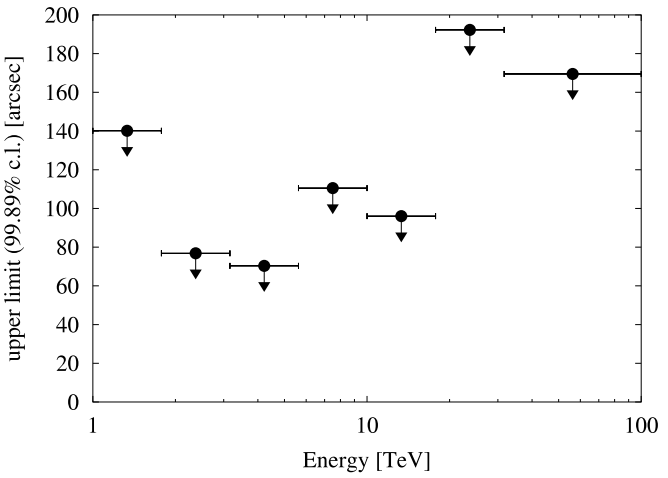

FIG. 5.—Upper limits (3 σ) for a Gaussian-type source size, calculated on the basis of the point-spread function predicted by simulations. These are independent (differential) upper limits, improving the sensitivity for a particular narrow (in energy) feature expected from an ionic component in the wind.

might have gone unnoticed in an analysis using the integral distribution of all gamma-ray events.

Taking all data, the center of the emission region is determined to be R.A. $= 5^{h}34^{m}31\overset{s}{.}1 \pm 0\overset{s}{.}2_{stat} \pm 1\overset{s}{.}8_{sys}$, decl. $= 22^{\circ}0'52'' \pm 3''_{stat} \pm 25''_{sys}$ (J2000.0), which is shifted by $12\overset{''}{.}4 \pm 3\overset{''}{.}1_{stat} \pm 25''_{sys}$ angular distance to the west of the nominal position of the pulsar, R.A. $= 5^{h}34^{m}31\overset{s}{.}97$, decl. $= 22^{\circ}0'52\overset{''}{.}1$ (J2000.0; Han & Tian 1999). This shift is consistent with the expectation based on the centroid position of the X-ray–emitting nebula. The centroid position of the X-ray–emitting nebula, derived from public *Chandra* data of the Crab excluding the pulsar emission, is shifted by 9″ to the west. In declination the position of the TeV emission region is consistent with the position of the pulsar, at an angular distance of $1\overset{''}{.}9 \pm 3\overset{''}{.}0_{stat} \pm 25''_{sys}$. The centroid position of the X-ray–emitting nebula, as measured with the *Chandra* X-ray telescope, is shifted to the north by 13″.

Checks on the data split into the yearly observation campaigns confirm the offset to be present throughout the observation time. The statistical uncertainty on the position is smaller than the observed shift in right ascension. However, given the systematic uncertainty of 25″ derived from the pointing calibration, it is not possible to identify the position of the emission region with the pulsar or with structures in the nebula. The shift remains constant for different energy bins, as shown in Figure 4.

The limits on the source extension σ_{src} (with a 99.865% c.l.) are shown in Figure 5. Clearly, a source size exceeding 2′ can be excluded at energies below 10 TeV. At higher energies, the limit given here constrains the size to be less than 3′. The expected source size in the leptonic model would be close to 20″, whereas for an ionic component the size of the emission region would exceed 3′. Given the upper limits here, a narrow (in energy) emission component, as predicted by Amato et al. (2003) and Bednarek & Bartosik (2003), which could lead to an increase of the source size for energies at which this emission component dominates, is not found. This is consistent with the upper limit derived on the fraction of the spin-down luminosity present in kinetic energy of ions in the wind (see § 5).

In Figure 6, the upper limit on the source extension between 3 and 5.6 TeV is compared with the radio (*gray scale*) and X-ray (*contours*) maps taken from the *Chandra* Supernova Remnant Catalog.[15] The solid circle indicates the upper limit on the TeV source size. The small white square depicts the position of the TeV emission centroid; the side length of the square indicates the statistical uncertainty on the position.

4.3. *Phase-resolved Analysis*

The phasogram obtained by folding the events registered from the direction of the Crab pulsar and a background region

[15] See http://snrcat.cfa.harvard.edu.

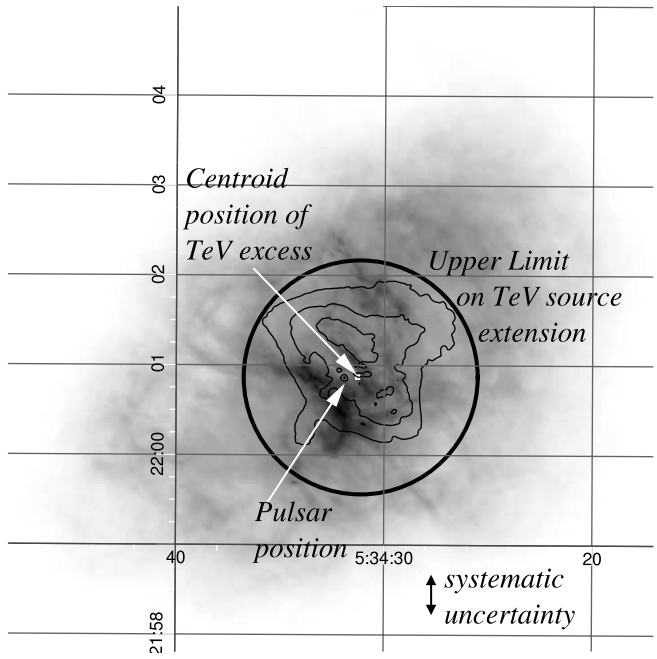

FIG. 6.—*Gray scale*: Radio map of the Crab Nebula, combined with X-ray contours. The circle indicates the upper limit on the TeV source size and the white square the position of the TeV centroid (the side length indicates the 3″ statistical error). [*See the electronic edition of the Journal for a color version of this figure.*]

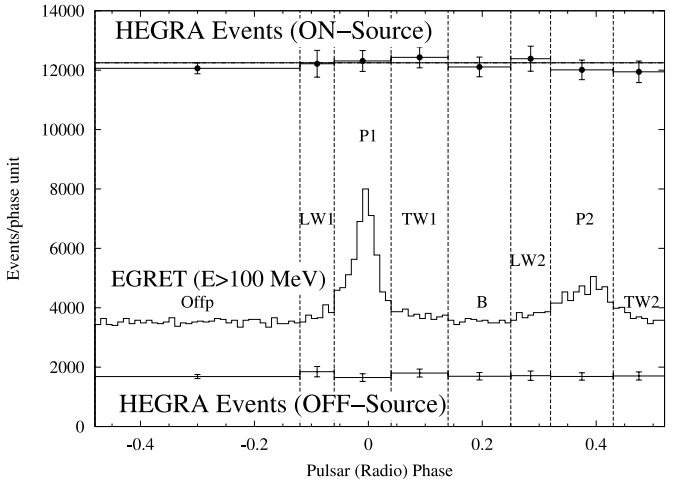

FIG. 7.—Phasogram of the Crab emission at two different energies: EGRET measurements show a bimodal distribution above 100 MeV. The different characteristic pulse intervals are marked (see text for further details). For the entire HEGRA data set, the on- and off-source distributions in the same phase bins are shown without evidence for a signal.

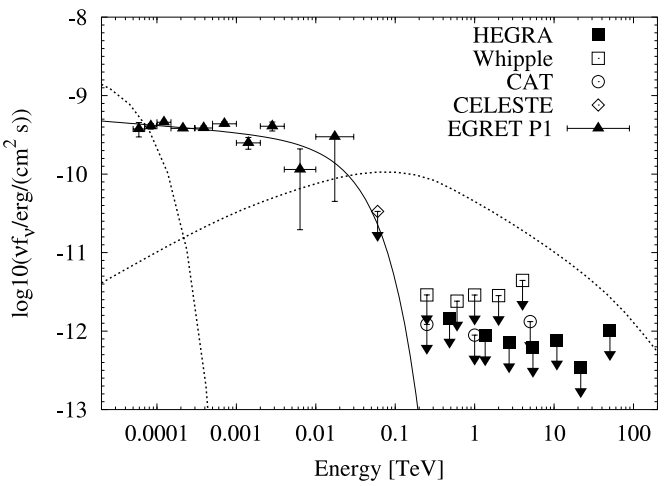

FIG. 8.—Result of a search for pulsed gamma-ray emission with HEGRA (filled squares indicate upper limits). The integral upper limits quoted for the CAT, CELESTE, and Whipple groups have been converted by assuming differential spectral indices of −2.4 at energies below 1 TeV and −2.6 above 1 TeV. For comparison, the energy spectrum for the main pulse, as detected by the EGRET spark chamber, is shown by upward-pointing triangles. The existence of a cutoff is expected in most theoretical models that propose the origin of the gamma rays to be close to the polar cap or the magnetosphere (outer gap). The upper limits shown are consistent with the picture of a cutoff at a few tens of GeV. The solid line is for a fit of a power-law function with photon index $\Gamma = -2.08$ and an exponential cutoff at 25 GeV to the EGRET data and the CELESTE upper limit, as suggested in Durand (2003). The dotted lines are for the synchrotron and inverse Compton emission of the nebula, as given by the model prediction explained in the text.

are shown in Figure 7, together with the phasogram obtained with EGRET at lower energies (Fierro et al. 1998). In addition, the search for pulsed emission is carried out on short data sets covering a month each. This is a test to check whether unnoticed long-term instability effects of the GPS timing information might have smeared a signal after data taken over long periods of time were combined. The distribution of probabilities derived from the various tests (Rayleigh and Z_2^2) is consistent with being uniform for on- and off-source data. No episodic excess is observed.

In the absence of a pulsed signal, upper limits are calculated. The strong, persistent signal of the Crab Nebula causes a substantial background to a possible pulsed signal and needs to be considered for the calculation of upper limits.

The method described in Aharonian et al. (1999a) is used to constrain a possible pulsed fraction of the unpulsed flux. Here we use the main pulse (P1) region between phases −0.06 and 0.04 to derive upper limits at the 99.865% c.l. (3 σ).

The upper limits for seven bins of energy are summarized in Table 4 and shown in Figure 8, together with results from EGRET (Fierro et al. 1998) and ground-based gamma-ray detectors CAT (Cerenkov Array at Themis; Musquère et al. 1999), Whipple (Lessard et al. 2000), and CELESTE (de Naurois et al. 2002). The HEGRA upper limits are marginally dependent on the assumed energy spectrum because they are calculated differentially for narrow energy bins. In order to compare these values with other published (integral) upper limits, a differential power law–type spectrum has been assumed. Notably, the HEGRA upper limits cover a wider energy range than the other results and reach the lowest value in this range. Furthermore, the upper limits are independent for each energy band, whereas all other quoted upper limits are integral limits that are less sensitive to narrow features in the spectrum.

TABLE 4
DIFFERENTIAL UPPER LIMITS ON PULSED EMISSION

$\langle E \rangle$ (TeV)	$E_{low} - E_{high}$ (TeV)	Fractional Limit (%)	Flux Limit [10^{-14} photons (cm^2 s TeV)$^{-1}$]
0.548	0.32–1.00	3.3	392.5
1.414	1.00–2.00	2.4	29.6
2.828	2.00–4.00	2.8	6.03
5.657	4.00–8.00	4.3	1.32
11.314	8.00–16.00	7.4	0.41
22.627	16.00–32.00	7.1	0.05
56.569	32.00–100.0	43.4	0.02

The model predictions for outer gap emission, as calculated recently by Hirotani & Shibata (2001), are partially excluded by the upper limits presented here. However, the expected flux from the Crab pulsar depends strongly on the opacity of the acceleration site for very high energy photons. The opacity is governed by the ambient soft photon density and the strength of the magnetic field. The optimistic cases considered, with the gap sufficiently far away from the pulsar and low ambient photon density, are nominally excluded by the upper limits given here. As has been pointed out (K. Hirotani 2004, private communication), further absorption of photons by single-photon pair production is expected and will reduce the expected flux considerably. The predictions of this model need to be revised and will not be constrained by this observation.

5. MODEL CALCULATIONS FOR THE EMISSION FROM THE NEBULA AND DISCUSSION

5.1. *Broadband Spectral Energy Distribution*

For the purpose of calculating the inverse Compton–scattered radiation, three basic photon fields need to be taken into account:

1. *Synchrotron emission*.—This radiation field dominates in density for all energies and is the most important seed photon field present.

2. *Far-infrared excess*.—Observations at far-infrared wavelengths have shown the presence of possibly thermal emission

that exceeds the extrapolation of the continuum emission from the radio band. This component is best described by a single temperature of 46 K (Strom & Greidanus 1992). Unfortunately, the spatial structure of the dust emission remains unresolved, which introduces uncertainties for the model calculations. We have assumed the dust to be distributed like the filaments, with a scale length of 1.′3. Sophisticated analyses of data taken with the *Infrared Space Observatory* (*ISO*) satellite indicates that the dust emission can be resolved (Green et al. 2004). The resulting size seems to be consistent with the value assumed here.

3. *Cosmic microwave background* (*CMB*).—Given the low energy of the CMB photons, scattering continues to take place in the Thomson regime even for electron energies exceeding 100 TeV (Aharonian & Atoyan 1995).

The influence of stellar light has been found to be negligible (Atoyan & Aharonian 1996). The optical line emission of the filaments is spatially too far separated from the inner region of the nebula, where the very energetic electrons are injected and cooled. However, in the case of acceleration taking place at different places in the nebula, the line emission could be important.

Given the recent detection of a compact component emitting millimeter radiation (Bandiera et al. 2002), this radiation field is included as seed photons for the calculation of the inverse Compton scattering. A simple model calculation has been performed that follows the phenomenological approach suggested by Hillas et al. (1998).

In brief, the observed continuum emission from the nebula up to MeV energies is assumed to be synchrotron emission. By setting the magnetic field to a constant average value within the nebula, a *prompt* electron spectrum can be constructed that reproduces the observed SED. Based on the measured size of the nebula at different wavelengths, the density of electrons and the produced synchrotron photons can be easily calculated in the approximation that the radial density profile follows a Gaussian distribution.

With this simple model, it is straightforward to introduce additional electron components and seed photon fields to calculate the inverse Compton–scattered emission of the nebula. The model is described in more detail by Horns & Aharonian (2004).

In order to extract the underlying electron spectrum, a broadband SED is required (see Fig. 9). For the purpose of compiling and selecting available measurements in the literature, mostly recent measurements have been chosen. The prime goal of the compilation is to cover all possible wavelengths from radio to gamma ray. The radio data are taken from Baars & Hartsuijker (1972) and references therein, millimeter data from Mezger et al. (1986) and Bandiera et al. (2002) and references therein, the infrared data obtained with *IRAS* in the far- to mid-infrared band from Strom & Greidanus (1992) and those with *ISO* in the adjacent mid- to near-infrared band from Douvion et al. (2001).

Optical and near-UV data from the Crab Nebula require some extra considerations. The reddening along the line of sight toward the Crab Nebula is a matter of some debate. For the sake of homogeneity, data in the optical (Véron-Cetty & Woltjer 1993) and near-UV and UV (Hennessy et al. 1992; Wu 1981) have been corrected applying an average extinction curve for $R = 3.1$ and $E(B - V) = 0.51$ (Cardelli et al. 1989).

The high-energy measurements of the Crab Nebula have been summarized recently in Kuiper et al. (2001), to the extent of including *ROSAT* HRI, *BeppoSAX* LECS, MECS, and PDS,

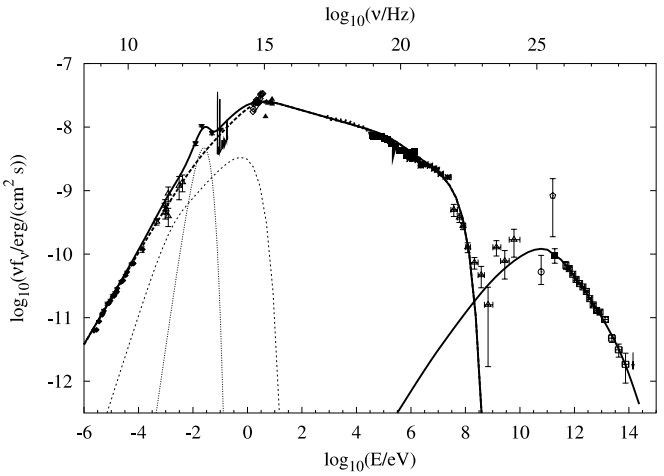

FIG. 9.—Calculations described in § 5 (*curves*). For a wide range of energies, recent measurements have been compiled from the literature (see the text for further details and references).

COMPTEL, and EGRET measurements covering the range from soft X-rays up to gamma-ray emission. For the intermediate range of hard X-rays and soft gamma-rays, data from the Earth occultation technique with the BATSE instrument have been included (Ling & Wheaton 2003).

The observations of the Crab Nebula at VHE ($E > 100$ GeV) have been carried out with a number of ground-based detectors. Most successfully, Cerenkov detectors have established the Crab Nebula as a standard candle in the VHE domain. A summary of the measurements is presented in Aharonian et al. (2000b). Recently, the MILAGRO group has published a flux estimate that is consistent with the measurement presented here (Atkins et al. 2003).

The results from different detectors reveal underlying systematic uncertainties in the absolute calibration of the instruments. To extend the energy range covered in this work (0.5–80 TeV), in Figure 9 results from nonimaging Cerenkov detectors, such as CELESTE (*open circle*), STACEE (*filled square*), and GRAAL (*open diamond*) at lower energy thresholds have been included (de Naurois et al. 2002; Oser et al. 2001; Arqueros et al. 2002), converted into a differential flux assuming a power law for the differential energy spectrum with a photon index of 2.4. For energies beyond 100 TeV, an upper limit on the integral flux from the CASA-MIA air shower array has been added (Borione et al. 1997) assuming a power law with a photon index of 3.2, as predicted from the model calculations.

The resulting broadband SED is shown in Figure 9, including as solid lines the synchrotron and inverse Compton emission, as calculated with the electron energy distribution assumed in this model. Also indicated as a dotted line in Figure 9 is the thermal excess radiation, which is assumed to follow a modified blackbody radiation distribution with a temperature of 46 K. Finally, the emission at millimeter wavelengths is indicated by a thin dashed line (see also § 5.2). The thick dashed line indicates the synchrotron emission excluding the thermal infrared and nonthermal millimeter radiation. The inverse Compton emission shown in Figure 9 includes the contribution from millimeter-emitting electrons (see § 5.2).

Besides the SED, an estimate of the volume of the emitting region is required to calculate the photon number density in the nebula to include as seed photons for inverse Compton

TABLE 5
PREDICTED INVERSE COMPTON DIFFERENTIAL ENERGY SPECTRUM FOR DIFFERENT SEED PHOTONS

ENERGY [log(E/TeV)]	TOTAL	COMPONENTS AS LABELED IN FIGURE 10				
		1	2	3	4	5
−2.3835	−5.5682	−5.9685	−6.4142	−6.5613	−6.5423	−6.1671
−2.2168	−5.8493	−6.2340	−6.6881	−6.8169	−6.8950	−6.4603
−2.0501	−6.1358	−6.5045	−6.9685	−7.0784	−7.2499	−6.7664
−1.8835	−6.4293	−6.7811	−7.2561	−7.3481	−7.6054	−7.0891
−1.7168	−6.7305	−7.0644	−7.5515	−7.6295	−7.9614	−7.4289
−1.5501	−7.0412	−7.3557	−7.8558	−7.9268	−8.3177	−7.7880
−1.3835	−7.3618	−7.6561	−8.1704	−8.2436	−8.6747	−8.1660
−1.2168	−7.6932	−7.9668	−8.4962	−8.5827	−9.0324	−8.5616
−1.0501	−8.0372	−8.2903	−8.8345	−8.9416	−9.3908	−8.9833
−0.8835	−8.3966	−8.6298	−9.1860	−9.3135	−9.7503	−9.4553
−0.7168	−8.7994	−8.9893	−9.5500	−9.6927	−10.1109	...
−0.5501	−9.1819	−9.3752	−9.9242	−10.0780	−10.4731	...
−0.3835	−9.5879	−9.7950	−10.3056	−10.4700	−10.8368	...
−0.2168	−10.0108	−10.2403	−10.6928	−10.8694	−11.2027	...
−0.0501	−10.4374	−10.6914	−11.0862	−11.2773	−11.5710	...
0.1165.....	−10.8674	−11.1465	−11.4859	−11.6941	−11.9421	...
0.2832.....	−11.3010	−11.6052	−11.8925	−12.1209	−12.3166	...
0.4499.....	−11.7378	−12.0673	−12.3060	−12.5583	−12.6950	...
0.6165.....	−12.1785	−12.5325	−12.7267	−13.0072	−13.0782	...
0.7832.....	−12.6235	−13.0008	−13.1547	−13.4685	−13.4669	...
0.9499.....	−13.0730	−13.4722	−13.5905	−13.9431	−13.8621	...
1.1165.....	−13.5277	−13.9470	−14.0343	−14.4318	−14.2652	...
1.2832.....	−13.9885	−14.4258	−14.4868	−14.9353	−14.6784	...
1.4499.....	−14.4571	−14.9100	−14.9494	−15.4541	−15.1047	...
1.6165.....	−14.9366	−15.4021	−15.4246	−15.9887	−15.5496	...
1.7832.....	−15.4319	−15.9060	−15.9118	−16.5408	−16.0182	...
1.9499.....	−15.9477	−16.4287	−16.4345	−17.1204	−16.5060	...
2.1165.....	−16.4827	−16.9703	−16.9751	−17.7492	−17.0073	...
2.2832.....	−17.0254	−17.5166	−17.5249	−18.3934	−17.5230	...

NOTE.—Table entries are in units of $\log_{10}[d\Phi/dE(\mathrm{cm}^2\ \mathrm{s\ TeV})]$.

scattering. The size of the nebula decreases monotonically with increasing photon energies, which is predicted in the framework of the MHD flow models (Atoyan & Aharonian 1996; Amato et al. 2000).

The result of the calculation for the inverse Compton emission are tabulated separately for the different contributions from the seed photon fields in Table 5. The table lists the differential flux in the commonly used units of photons $\mathrm{cm}^{-2}\ \mathrm{TeV}^{-1}\ \mathrm{s}^{-1}$, which can be converted directly into energy flux by multiplying by the squared energy. For convenience, Table 6 gives the coefficients for a polynomial parameterization of the energy flux as a function of energy in a double-logarithmic representation with a relative linear accuracy better than 4%.

TABLE 6
POLYNOMIAL COEFFICIENTS FOR A FIT TO THE TOTAL INVERSE COMPTON ENERGY FLUX

Coefficient	Value
p_0	-10.3531
p_1	-0.578559
p_2	-0.119778
p_3	0.542375×10^{-1}
p_4	-0.766819×10^{-2}
p_5	-0.660223×10^{-2}

NOTE.—The coefficient corresponds to the second column in Table 5 and is of the form $\log\{\nu f_\nu/[\mathrm{ergs\ (cm^2\ s)^{-1}}]\} = \sum_{i=0}^{5} p_i \log^i(E/\mathrm{TeV})$.

5.2. *Effect of a Compact Emission Region at Millimeter Wavelengths*

The recently found emission region at millimeter wavelengths (Bandiera et al. 2002) is more compact than the radio and optical emission regions. In the current calculation, this emission region is modeled by an additional synchrotron emission component with a Gaussian equivalent radial width of 36″, as derived from Figure 5 of Bandiera et al. (2002). The electrons radiating at millimeter wavelengths also produce an additional inverse Compton component at GeV energies that partially reduces the discrepancy between the observed and predicted gamma-ray emission between 1 and 10 GeV. As a note, in order to match the EGRET flux, the millimeter emission region would have to be roughly half (≈16″) the size used for this calculation.

As pointed out in Bandiera et al. (2002), a thermal origin is ruled out for several reasons, leaving the possibility of synchrotron emission. The origin of the millimeter-emitting electrons is unclear. Contrary to the common picture of a relic electron population that was possibly emitted at an earlier stage of the nebula's development (see also § 5 of Kennel & Coroniti 1984b for a discussion on the problems to produce such a radio component in the framework of the MHD flow model), the millimeter electrons are apparently confined to

or possibly injected into a volume similar to that of the soft X-ray–emitting electrons.

The extra component can be explained by a population of electrons with a minimum Lorentz factor of $\approx 10^4$ and a maximum Lorentz factor of $\approx 10^6$, with a power-law index p close to 2 ($dN/d\gamma = N_0\gamma^{-p}$). In order to inject such an electron distribution, a small-scale shock is required at a distance of $\approx 10^{14}$ cm from the pulsar. The maximum Lorentz factor reachable in the downstream region scales with the curvature radius of the shock. The minimum Lorentz factor, according to the Rankine-Hugoniot relations for a shock at 10^{14} cm, is $\approx 10^4$, provided that the spectral index is ≈ 2 for the particle distribution. In recent MHD calculations (Bogovalov & Khangoulian 2002; Komissarov & Lyubarsky 2003), the observed jet-torus morphology of the Crab Nebula is reproduced by invoking a modulation of the flow speed with $\sin^2\theta$ (θ is the polar angle with respect to the rotation axis of the pulsar). This assumption is motivated by the solution for the wind flow in the case of an oblique rotator, assuming a split monopole magnetic field configuration (Bogovalov 1999). According to the calculation of Komissarov & Lyubarsky (2003), a multilayered shock forms. In the proximity of the polar region, the shock would form close to the pulsar and could be responsible for the injection of millimeter-emitting electrons.

This shock region has remained undetected because of the angular proximity (10 mas) to the pulsar and the fact that the continuum emission is predominantly produced in the millimeter and submillimeter wavelength bands. The inner shock is in principle visible with high-resolution observations with interferometers at millimeter wavelengths.

Intriguingly, there is observational evidence for ongoing injection of electrons radiating at 5 GHz frequency that show moving, wisplike structures similar to the optical wisps (Bietenholz & Kronberg 1992; Bietenholz et al. 2001). The injection of radio- and millimeter-emitting electrons into the nebula could, e.g., take place at additional shocks much closer to the pulsar than the previously assumed $14''$.

The additional compact millimeter component is of importance for the inverse Compton component. The electron population with $\gamma = 10^4$–10^5, introduced here to explain the excess at millimeter wavelengths, produces via inverse Compton scattering gamma rays between 1 and 10 GeV. The contribution is rather small (10%) but could easily become comparable to that of the other components if the millimeter-emitting region is smaller than assumed here. In this case, the EGRET data points would be better described by the model. Moreover, the millimeter component contributes seed photons for inverse Compton scattering in the Thomson regime, which contributes substantially at energies of a few TeV.

The combined inverse Compton spectrum is shown in Figure 10, decomposed according to the different seed photons (synchrotron, IR, millimeter, and CMB) and the additional inverse Compton component from the millimeter-emitting electrons. Clearly, the synchrotron emission present in the nebula is the most important seed photon field present. At high energies ($E > 10$ TeV), the millimeter radiation contributes significantly to the scattered radiation.

5.3. *Comparison of the Model with Data*

The agreement of the calculated inverse Compton spectrum with the data is excellent (see Fig. 10). The only free parameter of the model calculation is the magnetic field, which in turn can be determined from the data by minimizing the χ^2 of the data (see § 5.4). The resulting value of χ^2 is slightly lower

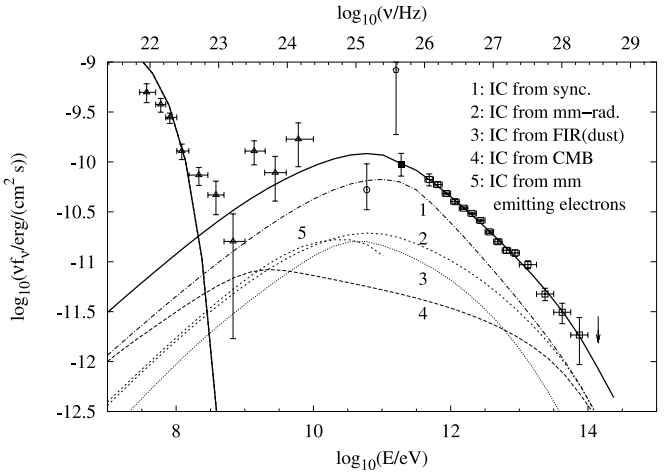

FIG. 10.—Inverse Compton spectrum decomposed into different components, as defined by the target seed photons. The synchrotron radiation dominates at all energies. However, the millimeter excess is of equal importance above 30 TeV. Eventually, beyond 100 TeV, the microwave background contributes significantly to the overall spectrum. Note that the contribution of the millimeter radiation dominates over the dust component at all energies. Also shown is the inverse Compton component from the electrons emitting the synchrotron millimeter radiation. The symbols are the same as for Fig. 9

than for the power-law fit: $\chi^2_{\rm red}({\rm dof}) = 0.96(14)$ for the inverse Compton model, as compared with $\chi^2_{\rm red}({\rm dof}) = 1.3(13)$. However, the small change in χ^2 does not convey the full information. The slope of the spectrum is expected to change slightly with energy for the inverse Compton model. For the purpose of testing this gradual softening predicted in the model, the differential power law was calculated from the data points by computing the slope between two data points with index i, j separated by 0.625 in decadic logarithm:

$$\Gamma(E) = \frac{\ln \Phi_i - \ln \Phi_j}{\ln E_i - \ln E_j}, \tag{4}$$

$$E = \exp\left[0.5\left(\ln E_i + \ln E_j\right)\right], \tag{5}$$

$$\sigma_\Gamma = \frac{\sqrt{\left(\sigma_{\Phi(i)}/\Phi_i\right)^2 + \left(\sigma_{\Phi(j)}/\Phi_j\right)^2}}{\ln E_i - \ln E_j}. \tag{6}$$

For the sake of simplicity, the error on E_i, E_j is ignored. The effect of including the statistical error on E_i, E_j is negligible. The interval of 0.625 in decadic logarithm gives sufficient leverage to calculate a reliable slope, and at the same time it is small enough to resolve the features. The expected slope is calculated from the model for both cases, including and excluding the millimeter seed photon field. The result is shown in Figure 11. The straight dashed line shows the predicted slope, as given by the parameterization of Hillas et al. (1998), and the open circles indicate the predictions from Aharonian & Atoyan (1998), which are consistent with the calculation described here. Note that the data points are independent. As is clearly seen, the expected and measured changes in slope agree nicely. The systematic and energy-dependent deviation from the constant photon index determined by the power-law fit is evident. Ignoring the millimeter component gives, on average, a slightly softer spectrum, with the same softening with increasing energy. It is remarkable how little the slope is expected to change over exactly the energy range covered by the observations. At energies below 200 GeV, a strong flattening

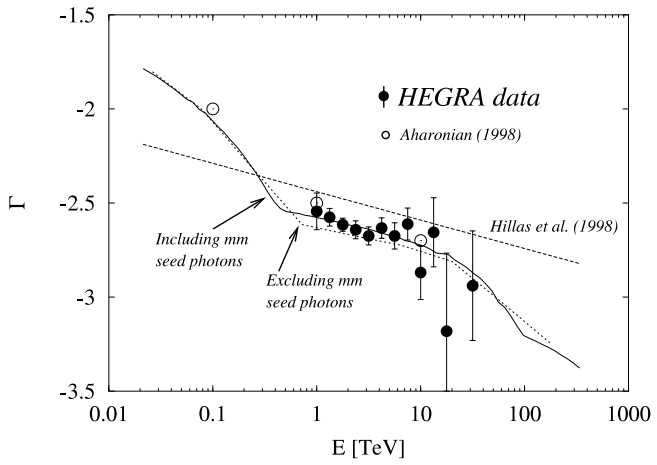

FIG. 11.—Predicted photon index (*line*), which changes only very little in the energy range considered and is consistent with the measured values (*filled circles*).

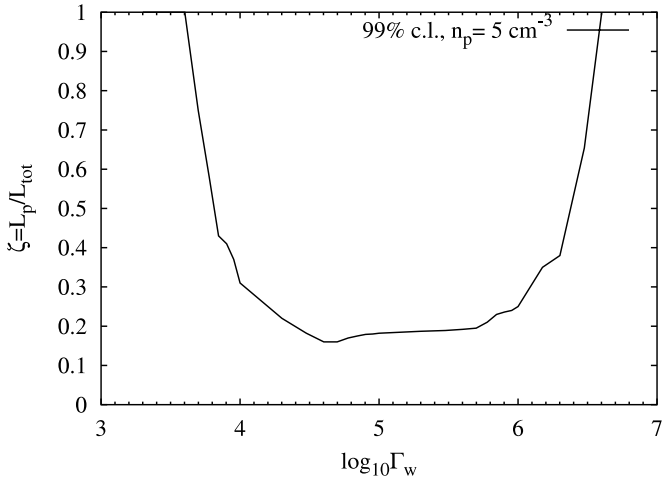

FIG. 12.—For a variety of bulk Lorentz speeds of the wind, the fraction of the total spin down power which is injected in the form of ions is constrained to be less than 20%. For Lorentz factors beyond 10^6 and below 10^4, a substantial fraction of the power could be present in the form of ions.

of the energy spectrum is to be expected. At the high-energy end, beyond roughly 70 TeV, the softening is expected to be stronger.

5.4. *The Average Magnetic Field*

The average magnetic field is calculated by minimizing the χ^2 of the model with respect to the data, varying the magnetic field as a free parameter. For every value for the magnetic field, the break energies and normalization of the electron spectrum are chosen to reproduce the synchrotron spectrum.

The resulting χ^2 as a function of magnetic field shows a minimum at 161.6 μG, with $\chi^2_{\rm red}({\rm dof}) = 0.96(14)$. The 1 σ statistical uncertainty of 0.8 μG is negligible. The systematic uncertainties of 15% on the absolute energy scale of the measurement translate into a systematic error on the average magnetic field of 18 μG.

5.5. *Gamma-Ray Emission from Ions in the Wind*

As has been pointed out independently by Amato et al. (2003) and Bednarek & Bartosik (2003), the presence of ions in the relativistic wind could be detected from the production of neutrinos and gamma rays in inelastic scattering processes with the matter in the nebula. Neutrinos and gamma rays would be produced as the decay products of charged and neutral pions. Both calculations show a similar signature for the ion-induced gamma-ray flux, which appears as a rather narrow feature in a νf_ν diagram. The presence of ions is required in acceleration models in which positrons in the downstream region are accelerated by cyclotron waves excited by ions (Arons 1995).

Qualitatively, the ions in the pulsar wind fill the nebula without undergoing strong energy losses. For a typical bulk velocity of the wind of $\Gamma = 10^6$, the dominant energy losses are adiabatic expansion of the nebula and escape of particles with typical timescales of the order of the age of the remnant. Therefore, the almost monoenergetic distribution of the ion energies as injected by the wind is not widened significantly.

From the model calculations described above, the TeV data are well explained by inverse Compton scattering of electrons present in the nebula. The shape and the absolute flux measured are consistent with the predictions of this model. However, an admixture of gamma-ray emission processes of electrons and ions could be possible. In an attempt to estimate how much of the spin-down power of the pulsar could be present in the form of ions, a model calculation for the gamma-ray emission from ions in the wind is performed. Here, 99% c.l. upper limits are calculated on the fraction ζ of the spin-down luminosity present in ions ($L_{\rm ion} = \zeta \dot{E}_{\rm pulsar}$) by adding the additional component to the inverse Compton component and comparing this prediction with the data. The χ^2 of the combined prediction is calculated for different values of ζ until the χ^2 increases by $\Delta\chi^2 = 29.15$ for a 99% c.l. This calculation is repeated for various values of Γ.

The calculation of the gamma-ray flux from the ions depends on a few simplifications. It is assumed that the ions are predominantly protons with a narrow energy distribution with $E_p \approx \Gamma m_p c^2$. For the injection rate of protons $\dot{N}_p = \zeta \dot{E}_{\rm pulsar}/E_p$, with $\dot{E}_{\rm pulsar} = 5 \times 10^{38}$ ergs s^{-1}, is assumed. The injection rate of π^0 depends on the conversion efficiency, $\dot{N}_\pi = f_\pi \dot{N}_p$. The conversion efficiency f_π of the protons to π^0 is given by the ratio of energy-loss timescales for *pp* scattering and escape/adiabatic losses. Assuming an average number density of the gas in the nebula of 5 cm^{-3}, the conversion efficiency is 5.4×10^{-5}.

The upper limits for ζ as a function of the bulk Lorentz factor are given in Figure 12. Clearly, for bulk Lorentz factors between 10^4 and 10^6, only a small fraction of the energy carried by the wind could be present in the form of ions (<20%). For Lorentz factors beyond 10^6 or smaller than 10^4, a substantial part of the power could be injected in the form of ions.

However, the assumption of a narrow energy distribution might not be true. In the case of a variation of the wind speed, as discussed above in the context of a split magnetic monopole model, the injected ions could have a wider distribution in energy, which subsequently makes an identification of this feature in the measured gamma-ray spectrum more complicated and the upper limits calculated less restrictive.

5.6. *Additional Components*

The presence of additional electron populations in the nebula with $\gamma > 10^5$ can be constrained by the gamma-ray data presented here. Obviously, the observed synchrotron emission already excludes the presence of components not accounted for in the model calculations presented in § 5. However, the frequency interval between hard UV and soft X-ray emission is

not covered by observations, and large systematic uncertainties on the strong absorption present would in principle not exclude the presence of an additional component that is sufficiently narrow in energy. Specifically, electrons following a relativistic Maxwellian-type distribution may form in the framework of specific acceleration models (Hoshino et al. 1992). For the magnetic field of 161 μG, UV-emitting electrons would have $\gamma \approx 10^7$. Given the age of the nebula, 954 yr, the synchrotron-cooled spectrum is close to a power law with $dN/d\gamma \propto \gamma^{-2}$, reaching to $\gamma_{\min} = 10^6$. The resulting synchrotron emission is not in conflict with the available data unless the power in the extra Maxwellian-type injection spectrum becomes a sizable fraction ($L_{\rm Maxw}/L_{\rm tot} > 0.3$) of the total power of the electrons responsible for the broadband SED. However, after calculating the inverse Compton emission of this extra component and comparing it with the gamma-ray data, an upper limit at 99% c.l. can be set, $L_{\rm Maxw}/L_{\rm tot} < 0.04$, ruling out the existence of unnoticed (unobserved) electron populations with $\gamma = 10^6 - 10^7$ in the nebula. The possible existence of an additional synchrotron-emitting component, possibly associated with a spectral hardening in the MeV energy range, as observed consistently by the COMPTEL instrument (Much et al. 1995), BATSE (Ling & Wheaton 2003), and INTEGRAL (Roques et al. 2003), has been discussed, e.g., in de Jager (2001). The contribution of such an additional component to the observed TeV flux is probably small and is relevant only at energies exceeding a few hundred TeV.

6. SUMMARY AND CONCLUSIONS

The HEGRA stereoscopic system of air Cerenkov telescopes performed extensive observation of the Crab supernova remnant. The energy spectrum has been determined over more than 2 decades in energy and 5 decades in flux. The main point of the data analyses is to constrain the acceleration of electron/positron pair plasma in the vicinity of the termination shock of the pulsar wind in the surrounding medium. The high-energy data presented here give a unique view on the extreme accelerator that resides in the Crab Nebula.

The energy spectrum of the unpulsed component is very likely produced by the same electrons that produce the broadband emission spectrum extending from soft to hard X-rays and finally reach the soft gamma rays (with a cutoff at a few MeV). The electrons upscatter mainly photons of the synchrotron nebula, the soft thermal photons seen as the far-infrared excess, the universal cosmic microwave background (CMB), and possibly millimeter radiation emitted in a rather compact region.

The comparison of the flux level at TeV energies, combined with the synchrotron flux in a simple spherical model, constrains directly the magnetic field in the emission region of the nebula to be at the level of 160 μG. The agreement of the measured broadband energy spectrum ranging from soft X-rays up to 100 TeV with the prediction based on a simple model of an electron population being injected at the standing reverse shock strengthens the claim that electrons with energies exceeding 10^{15} eV are continuously accelerated. Limited by the photon statistics detected at high energies (>10 TeV), expected variations in the acceleration/cooling rate on timescales of months for these electrons cannot be established with the current instrumentation.

The data show evidence for the predicted gradual softening of the energy spectrum. Below roughly 200 GeV the spectrum is expected to harden quickly. Future detectors with a sufficiently low energy threshold will be able to see this feature. However, the expected *softening* occurs rapidly at energies beyond 70 TeV. Here low-elevation observations with the Cerenkov telescopes from the southern hemisphere will be very helpful.

Given the good agreement of the predicted inverse Compton spectrum with the measurement, either the presence of ions in the wind is negligible or radiative losses are exceedingly small. Independent of the spectrum, the morphology of the emission region could reveal signatures of the presence of ions in the wind and the nebula. Experimental upper limits given here constrain the size of the emission region at the considered energies to be less than $2'$, and less than $3'$ above 10 TeV. This excludes, for example, a strong contribution from the outer shock of the (undetected) expanding supernova remnant and constrains the transport of ions in the wind.

Finally, pulsed emission from inside the pulsar's magnetosphere at high energies is expected in outer gap models. A dedicated search for narrow features, as predicted in this type of model, has been performed, and in the absence of a signal, upper limits have been calculated. The upper limits reach well below the more optimistic predictions of Hirotani & Shibata (2001), but more recent calculations indicate that the pair opacity in the emission region is possibly larger than originally anticipated. In a different scenario, pulsed emission is expected to arise as a consequence of inverse Compton scattering of pulsed soft photons by the unshocked wind (Bogovalov & Aharonian 2000). The upper limits derived here are useful in constraining combinations of the bulk Lorentz factor and the distance of wind injection to the pulsar. For a range of bulk Lorentz factors from 10^5 to 10^7 the distance of the wind is constrained to be accelerated more than 50 light radii away from the pulsar.

7. OUTLOOK

Future observations of the nebula with low energy threshold instruments (MAGIC, *GLAST*) and large collection area observations at small elevations from the southern hemisphere (CANGAROO III, HESS) should extend the accessible energy range below 100 GeV (MAGIC) and beyond 100 TeV (CANGAROO III, HESS), where the spectral shape is expected to deviate strongly from a power law with $\Gamma = -2.6$. With low energy threshold Cerenkov telescopes like MAGIC, the detection of pulsed emission from the pulsar becomes feasible. Combining information about possible variability of the nebula's emission at different wavelengths (specifically, hard X-rays and, e.g., 20–100 TeV emission) would ultimately prove the common (electronic) origin of the observed emission. Fortunately, the Crab will be frequently observed as a calibration source by all Cerenkov telescopes and by *INTEGRAL* and other future hard X-ray missions, so that even without dedicated observations, substantial observation time will be accumulated. A dedicated millimeter observation with subarcsecond resolution of the region of the nebula within the X-ray torus would be of great interest in order to confirm the predicted existence of multilayered shocks that could be responsible for the millimeter emission detected with the moderate-resolution (>10″) observations currently available. If the injection of millimeter-emitting electrons in a compact region is confirmed, inverse Compton–scattered emission produced by the same low-energy electrons could in principle explain the discrepancy of the model with the energy spectrum observed by the EGRET spark chamber on board the *CGRO*

satellite. Again, future observations with the *GLAST* satellite with improved statistics will be of great interest in studying the actual shape of the energy spectrum above a few GeV.

The support of the German ministry for research and technology (BMBF) and of the Spanish Research Council (CICYT) is gratefully acknowledged. G. R. acknowledges receipt of a Humboldt fellowship. We thank the Instituto de Astrofísica de Canarias for the use of the site and for supplying excellent working conditions at La Palma. We thank K. Hirotani, Y. Gallant, S. Bogovalov, D. Khangoulian, and O. Skjæraasen for inspiring discussions. We acknowledge the support of the Jodrell Bank pulsar team for providing us with the ephemerides of the Crab pulsar and A. Franzen for letting us analyze the optical data taken with the HESS telescopes on the Crab pulsar. This research has made use of NASA's Astrophysics Data System Bibliographic Services and the *Chandra* X-Ray Center. We thank the anonymous referee for his suggestions to improve the manuscript.

REFERENCES

Aharonian, F. A. 1993, Towards a Major Atmospheric Cherenkov Detector, ed. R. C. Lamb (Ames: Iowa State Univ.), 81
———. 2000, NewA, 5, 377
Aharonian, F. A., & Atoyan, A. M. 1995, Astropart. Phys., 3, 275
———. 1998, in Neutron Stars and Pulsars, ed. N. Shibazaki, N. Kawai, S. Shibata, & T. Kifune (Tokyo: Universal Academy Press), 439
Aharonian, F., et al. 1999a, A&A, 346, 913
———. 1999b, A&A, 349, 11
———. 2000a, A&A, 361, 1073
———. 2000b, ApJ, 539, 317
———. 2000c, ApJ, 543, L39
———. 2001a, A&A, 370, 112
———. 2001b, A&A, 375, 1008
———. 2002a, A&A, 393, L37
———. 2002b, A&A, 393, 89
———. 2002c, A&A, 395, 803
———. 2003a, A&A, 403, 523
———. 2003b, A&A, 406, L9
Amato, E., Guetta, D., & Blasi, P. 2003, A&A, 402, 827
Amato, E., Salvati, M., Bandiera, R., Pacini, F., & Woltjer, L. 2000, A&A, 359, 1107
Arons, J. 1995, in ASP Conf. Ser. 72, Millisecond Pulsars: A Decade of Surprise, ed. A. S. Fruchter, M. Tavani, & D. C. Backer (San Francisco: ASP), 257
Arqueros, F., et al. 2002, Astropart. Phys., 17, 293
Atkins, R., et al. 2003, ApJ, 595, 803
Atoyan, A. M., & Aharonian, F. A. 1996, MNRAS, 278, 525
Baars, J. W. M., & Hartsuijker, A. P. 1972, A&A, 17, 172
Bandiera, R., Neri, R., & Cesaroni, R. 2002, A&A, 386, 1044
Bednarek, W., & Bartosik, M. 2003, A&A, 405, 689
Bennett, K., et al. 1977, A&A, 61, 279
Bietenholz, M. F., Frail, D. A., & Hester, J. J. 2001, ApJ, 560, 254
Bietenholz, M. F., & Kronberg, P. P. 1992, ApJ, 393, 206
Blackman, E. G., & Perna, R. 2004, ApJ, 601, L71
Bogovalov, S. V. 1999, A&A, 349, 1017
Bogovalov, S. V., & Aharonian, F. A. 2000, MNRAS, 313, 504
Bogovalov, S. V., & Khangoulian, D. V. 2002, MNRAS, 336, L53
Borione, A., et al. 1997, ApJ, 481, 313
Buccheri, R., et al. 1983, A&A, 128, 245
Bulian, N., et al. 1998, Astropart. Phys., 8, 223
Cardelli, J. A., Clayton, G. C., & Mathis, J. S. 1989, ApJ, 345, 245
Cheng, K. S., Ho, C., & Ruderman, M. 1986, ApJ, 300, 500
Coroniti, F. V. 1990, ApJ, 349, 538
Daum, A., et al. 1997a, Astropart. Phys., 8, 1
———. 1997b, Proc. 25th Int. Cosmic Ray Conf. (Durban), 5, 121
de Jager, O. C. 2001, in AIP Conf. Proc. 558, High Energy Gamma-Ray Astronomy, ed. F. A. Aharonian & H. J. Völk (Melville: AIP), 154
de Jager, O. C., Swanepoel, J. W. H., & Raubenheimer, B. C. 1989, A&A, 221, 180
de Naurois, M., et al. 2002, ApJ, 566, 343
Dombrovsky, V. A. 1954, Dokl. Akad. Nauk SSSR, 94, 1021
Douvion, T., Lagage, P. O., Cesarsky, C. J., & Dwek, E. 2001, A&A, 373, 281
Durand, E. 2003, Thèse de doctorat, Univ. Sciences et Technologies, Bordeaux I
Fierro, J. M., Michelson, P. F., Nolan, P. L., & Thompson, D. J. 1998, ApJ, 494, 734
Franzen, A., Gillessen, S., Hermann, G., & Hinton, J. 2003, Proc. 28th Int. Cosmic Ray Conf. (Tsukuba), 5, 2987
Gallant, Y. A., & Arons, J. 1994, ApJ, 435, 230
Green, D. A., Tuffs, R. J., & Popescu, C. C. 2004, MNRAS, in press
Han, J. L., & Tian, W. W. 1999, A&AS, 136, 571
Harding, A. K., Tademaru, E., & Esposito, L. W. 1978, ApJ, 225, 226
Hemberger, M. 1998, Ph.D. thesis, Univ. Heidelberg
Hennessy, G. S., et al. 1992, ApJ, 395, L13
Hermann, G. 1995, Towards a Major Atmospheric Cherenkov Detector IV, ed. M. Cresti (Piazzola sul Brenta: Papergraf), 396
Hester, J. J., et al. 1995, ApJ, 448, 240
———. 2002, ApJ, 577, L49
Hillas, A. M., et al. 1998, ApJ, 503, 744
Hirotani, K., & Shibata, S. 2001, ApJ, 558, 216
Hofmann, W. 2003, Astropart. Phys., 20, 1
Hofmann, W., Jung, I., Konopelko, A., Krawczynski, H., Lampeitl, H., & Pühlhofer, G. 1999, Astropart. Phys., 12, 135
Hofmann, W., Lampeitl, H., Konopelko, A., & Krawczynski, H. 2000, Astropart. Phys., 12, 207
Horns, D., & Aharonian, F. A. 2004, Proc. 5th INTEGRAL Workshop (ESA SP-552; Noordwijk: ESA), in press
Horns, D., et al. 2003, Proc. 28th Int. Cosmic Ray Conf. (Tsukuba), 5, 2373
Hoshino, M., Arons, J., Gallant, Y. A., & Langdon, A. B. 1992, ApJ, 390, 454
James, F. 1998, MINUIT Reference Manual (CERN Program Library Long Writeup D506; Geneva: CERN)
Kennel, C. F., & Coroniti, F. V. 1984a, ApJ, 283, 694
———. 1984b, ApJ, 283, 710
Kirk, J. G., & Skjæraasen, O. 2003, ApJ, 591, 366
Kohnle, A., et al. 1996, Astropart. Phys., 5, 119
Komissarov, S. S., & Lyubarsky, Y. E. 2003, MNRAS, 344, L93
Konopelko, A., Lucarelli, F., Lampeitl, H., & Hofmann, W. 2002, J. Phys. G, 28, 2755
Konopelko, A., & Plyasheshnikov, A. 2000, Nucl. Instrum. Methods Phys. Res. A, 450, 419
Kuiper, L., Hermsen, W., Cusumano, G., Diehl, R., Schönfelder, V., Strong, A., Bennett, K., & McConnell, M. L. 2001, A&A, 378, 918
Lessard, R. W., et al. 2000, ApJ, 531, 942
Li, T.-P., & Ma, Y.-Q. 1983, ApJ, 272, 317
Ling, J. C., & Wheaton, W. A. 2003, ApJ, 598, 334
Lucarelli, F., Konopelko, A., Aharonian, F., Hofmann, W., Kohnle, A., Lampeitl, H., & Fonseca, V. 2003, Astropart. Phys., 19, 339
Lyne, A. G., Jordan, C. A, & Roberts, M. E. 2003, Jodrell Bank Crab Pulsar Monthly Ephemeris, http://www.jb.man.ac.uk/~pulsar/crab.html
Mardia, K. V. 1972, Statistics of Directional Data (London: Academic Press)
Mezger, P. G., Tuffs, R. J., Chini, R., Kreysa, E., & Gemünd, H.-P. 1986, A&A, 167, 145
Mohanty, G., et al. 1998, Astropart. Phys., 9, 15
Mori, K., Burrows, D. N., Hester, J. J., Pavlov, G. G., Shibata, S., & Tsunemi, H. 2004, ApJ, 609, 186
Much, R., et al. 1995, A&A, 299, 435
Musquère, A., et al. 1999, Proc. 26th Int. Cosmic Ray Conf. (Salt Lake City), 3, 460
Nolan, P. L., et al. 1993, ApJ, 409, 697
Oña-Wilhelmi, E., et al. 2003, Proc. 28th Int. Cosmic Ray Conf. (Tsukuba), 4, 2449
Oser, S., et al. 2001, ApJ, 547, 949
Pacini, F., & Salvati, M. 1973, ApJ, 186, 249
Pitjeva, E. V. 2001, Celest. Mech. Dyn. Astron., 80, 249
Pühlhofer, G., et al. 2003a, Astropart. Phys., 20, 267
———. 2003b, Proc. 28th Int. Cosmic Ray Conf. (Tsukuba), 4, 2319
Rees, M. J., & Gunn, J. E. 1974, MNRAS, 167, 1
Roques, J. P., et al. 2003, A&A, 411, L91
Rowell, G. P. 2003, A&A, 410, 389
Scargle, J. D. 1969, ApJ, 156, 401
Shapiro, I. I. 1964, Phys. Rev. Lett., 13, 789
Shklovskii, I. S. 1953, Dokl. Akad. Nauk SSSR, 90, 983 (English transl. with commentary 1979, in A Source Book in Astronomy and Astrophysics, 1900–1975, ed. K. R. Lang & O. Gingerich, O. [Cambridge: Harvard Univ. Press], 488)
Sommers, P., & Elbert, J. 1987, J. Phys. G, 13, 553

Spitkovsky, A., & Arons, J. 2004, ApJ, 603, 669
Standish, E. M., Jr. 1982, A&A, 114, 297
———. 1998, JPL Planetary and Lunar Ephemerides (JPL IOM 312, F-98-048; Pasadena: JPL)
Stephenson, F. R., & Green, D. A. 2002, Historical Supernovae and Their Remnants (Oxford: Clarendon Press)
Strom, R. G., & Greidanus, H. 1992, Nature, 358, 654
Tanimori, T., et al. 1998, ApJ, 492, L33
Vacanti, G., Fleury, Y., Jiang, Y., Paré, E., Rovero, A. C., Sarazin, X., Urban, M., & Weekes, T. C. 1994, Astropart. Phys., 2, 1
Véron-Cetty, M. P., & Woltjer, L. 1993, A&A, 270, 370
Weekes, T. C., et al. 1989, ApJ, 342, 379
Weisskopf, M. C., et al. 2000, ApJ, 536, L81
Wu, C.-C. 1981, ApJ, 245, 581